Energy Conversion and Management 248 (2021) 114819

Contents lists available at ScienceDirect

Energy Conversion and Management

journal homepage: www.elsevier.com/locate/enconman

Characteristics of in-cylinder flow and mixture formation in a high-pressure spray-guided gasoline direct-injection optically accessible engine using PIV measurements and CFD

Donghwan Kim [a], Jisoo Shin [a], Yousang Son [b], Sungwook Park [c,*]

[a] Department of Mechanical Convergence Engineering, Graduate School of Hanyang University, Seoul 04763, Republic of Korea
[b] Engine Advanced Development Team, Hyundai Motor Group, Gyeonggi-do 18280, Republic of Korea
[c] School of Mechanical Engineering, Hanyang University, Seoul 04763, Republic of Korea

ARTICLE INFO

Keyword:
Spray-guided DI engine
Optically accessible engine
In-cylinder flow
Mixture formation
PIV measurements
CFD

ABSTRACT

In this study, a spray-guided gasoline direct-injection 2-cylinder optically accessible engine was used to analyze the characteristics of the in-cylinder flow and mixture formation using PIV measurements and computational fluid dynamics (CFD; CONVERGE v2.4). The mean velocity, tumble ratio, turbulent kinetic energy, and tumble center were calculated to quantify the characteristics of the in-cylinder flow. Moreover, flow rotation intensity was defined to evaluate the in-cylinder flow depending on the crank angle. In the early stage of the intake stroke, the intake air flowed into the cylinder with high momentum and velocity. Subsequently, tumble flow was generated in the middle stage of the intake stroke, and weak in-cylinder flow occurred during the compression stroke owing to the dissipation of momentum. The fuel injection caused intensification of the in-cylinder flow, increasing the in-cylinder flow velocity, tumble ratio, and turbulent kinetic energy. Furthermore, mixture formation was affected by the end of the injection timing and its characteristics were classified into homogeneous, stratified, and mal-distribution mixtures, depending on the region to which the end of injection timing belonged.

1. Introduction

Although many countries are focusing on the use of hybrid electric vehicles (HEVs) [1,2], pure electric vehicles (PEVs) [3], and fuel cell vehicles (FCVs) [4], immediate replacement of internal combustion engines (ICEs) is challenging owing to the limitations such as battery life, lack of charging stations, and limited mileage range [5]. According to Dudely et al., ICEs are estimated to be a major power source for passenger vehicles within the next 20 years [6]. However, owing to stricter emission regulations for ICEs, researchers have been continuously studying the combustion mode of ICEs. Conventional spark ignition (SI) engines operate under conditions with premixed and stoichiometric air–fuel mixture formation. The injection modes applicable are port fuel injection (PFI) and direct injection (DI) using a side-mounted injector [7]. However, satisfying future strict emission regulations using the conventional combustion mode is challenging. The air and fuel mixing performances can be increased through center injection. Various injection strategies can be applied because the injection is located near the spark plug, so that the flame propagation is directly influenced by the injection strategy. Therefore, various engines that apply the new combustion mode using a center-mounted injector have been researched.

For example, center injection is applied in spray-guided stratified charge (SGSC) engines to form an adequately stratified mixture near the spark timing. The SGSC engine is operated under lean conditions, resulting in several advantages such as reduced pumping losses, lower gas temperatures, and higher thermal efficiencies [8]. However, there are certain drawbacks such as wall wetting and fuel impingement, which can lead to instability combustion and pool fires due to the advanced injection timing [9]. In homogeneous charge compression ignition (HCCI) engines utilizing spontaneous auto-ignition combustion, a port fuel injector or center-mounted injector is used [10] and its operation involves relatively lower soot or NO_X emissions [11]. However, the HCCI engine suffers from certain problems, such as controlled auto-ignition timing [12,13], combustion phase [14], knocking and noise [15], operation range limitations, and homogeneous charge preparation. Among the many factors that induce problems in new combustion mode engines, a primary factor that determines engine performance is the air–fuel mixture formation [16,17]. Mixture formation is closely

* Corresponding author at: School of Mechanical Engineering, Hanyang University, 222 Wangsimni-ro, Seongdong-gu, Seoul 04763, Republic of Korea.
E-mail address: parks@hanyang.ac.kr (S. Park).

https://doi.org/10.1016/j.enconman.2021.114819
Received 5 August 2021; Accepted 27 September 2021
Available online 7 October 2021

Nomenclature

P_{amb}	Ambient pressure
P_{inj}	Injection pressure

Abbreviations

ASOE	After Start of Energizing
ASOI	After Start of Injection
aTDC	After Top Dead Center
bTDC	Before Top Dead Center
CFD	Computational Fluid Dynamics
CVC	Constant Volume Chamber
DI	Direct Injection
EOI	End of Injection
FCVs	Fuel Cell Vehicles
FFT	Fast Fourier Transform
GDI	Gasoline Direct Injector
HCCI	Homogeneous Charge Compression Ignition
HEVs	Hybrid Electric Vehicles
IC	Internal Combustion
ICE	Internal Combustion Engine
NA	Naturally Aspirated
PEVs	Pure Electric Vehicles
PFI	Port Fuel Injection
PIV	Particle Image Velocimetry
SGSC	Spray-Guided Stratified Charge
SI	Spark Ignition
SMD	Sauter Mean Diameter
SOE	Start of Energizing
TDC	Top Dead Center
TKE	Turbulent Kinetic Energy
TR	Tumble Ratio
WOT	Wide-Open Throttle

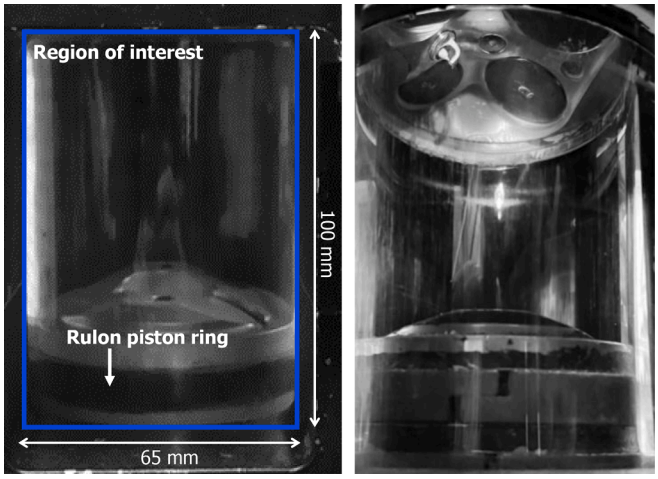

Fig. 1. Image of a transparent combustion chamber with quartz: (a) front view and (b) diagonal view.

Table 1
Specifications of the optically accessible engine.

Items	Details
Bore (mm)	75.6
Radius of crank (mm)	41.6
Stroke (mm)	83.38
Displacement volume per two cylinders (cc)	748.5
Length of con-rod (mm)	147.8
Compression height (mm)	27.5
Height of block (mm)	217.0
Piston topping (mm)	0.33
Crank offset (mm)	10
Piston pin offset (mm)	0.7
Stroke/bore ratio (-)	1.10
Compression ratio (-)	14
Intake valve open (bTDC°)	332
Intake valve close (bTDC°)	114
Exhaust valve open (aTDC°)	152
Exhaust valve close (aTDC°)	370

related to the characteristics of the in-cylinder flow and injection strategy [18,19], and is directly related to power, fuel consumption, and emissions [20,21]. Therefore, many researchers and engineers have focused on analyzing the interactions between the injected fuel and in-cylinder flow using particle image velocimetry (PIV) measurements and computational fluid dynamics (CFD).

Zeng et al. studied the spray-enhanced swirl flow for combustion stabilization in a SGSC DI SI engine employing a PIV imaging technique [22] and found that fuel injection causes a redistribution of the angular momentum resulting from spray-swirl interactions and a redistribution of the gas phase swirl flow. Therefore, the in-cylinder flow comprises a very repeatable vortex with a high angular momentum, leading to a decrease in the cycle-to-cycle variation. Geschwindner et al. investigated the interaction between in-cylinder flow and spray in an optically accessible engine with two spray-guided direct injections [23]. They acquired bulk in-cylinder flow using a PIV image technique and spray and demonstrated that the in-cylinder flow is heavily disturbed by the spray, which is injected at a later time, and the tumble flow can barely maintain its initial momentum by injection when the tumble is weak. Moreover, they emphasized the importance of a later flow structure for preventing spray collapse. In addition, they observed that increasing the in-cylinder flow magnitudes enhanced the spray-shape stability. Hill et al. studied the spray-induced turbulence in a DI optically accessible engine with a hollow cone injector using tomographic PIV [24]. They focused on the manner in which turbulent flow features, such as the turbulent kinetic energy (TKE), strain rate, and vorticity, evolved into the surrounding flow field. Costa et al. investigated in-cylinder flow in the absence of fuel injection during intake and compression strokes in a single-cylinder optically accessible engine [25]. The PIV measurement was performed at the partial region of the cylinder under three different engine speeds: 1,000, 1,500, and 2,000 rpm, while CFD simulations were conducted at 1,000 rpm. They quantified the characteristics of the in-cylinder flow, including the kinetic energy, TKE, and tumble vortex center position. Consequently, utilizing these PIV data results, they performed a CFD simulation based on the simulation model.

Several previous studies have focused on new combustion modes that apply center injection using PIV and CFD. However, research including both experiments and simulations regarding the correlation between the in-cylinder flow and spray has been limited and is needed to fully understand the characteristics of in-cylinder flow under various operating conditions. Furthermore, ICEs still require research regarding fuel efficiency, performance improvements, and exhaust reduction methods in the future. Thus, in this study, we analyzed the in-cylinder flow characteristics of a DI engine with a spray-guided injector, which is the most fundamental step for optimizing engine design and control factors. The effects of fuel injection on in-cylinder flow were observed by employing single injection instead of multiple injection, depending on the injection timing. Moreover, the mixture formation, depending on the injection timing, was analyzed using CFD.

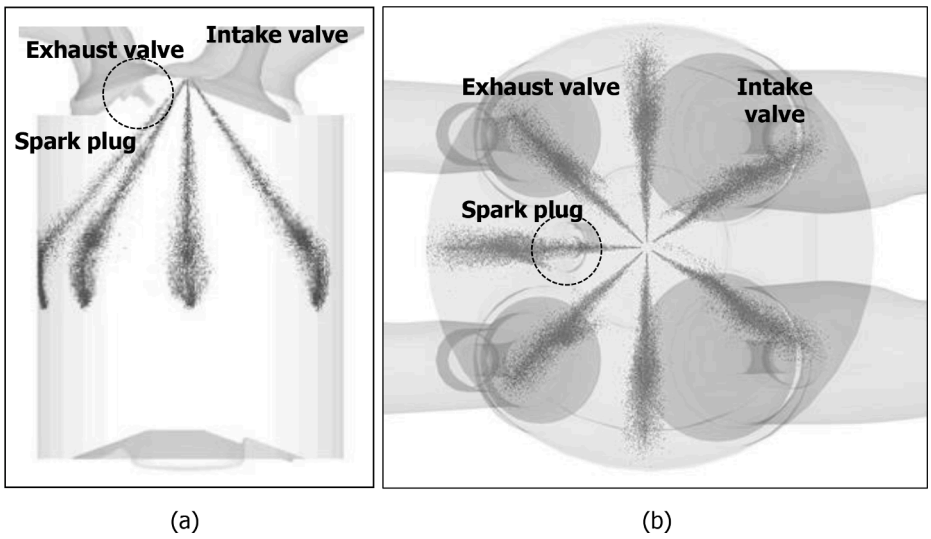

Fig. 2. Spray structure and spark plug location: (a) front view and (b) top view.

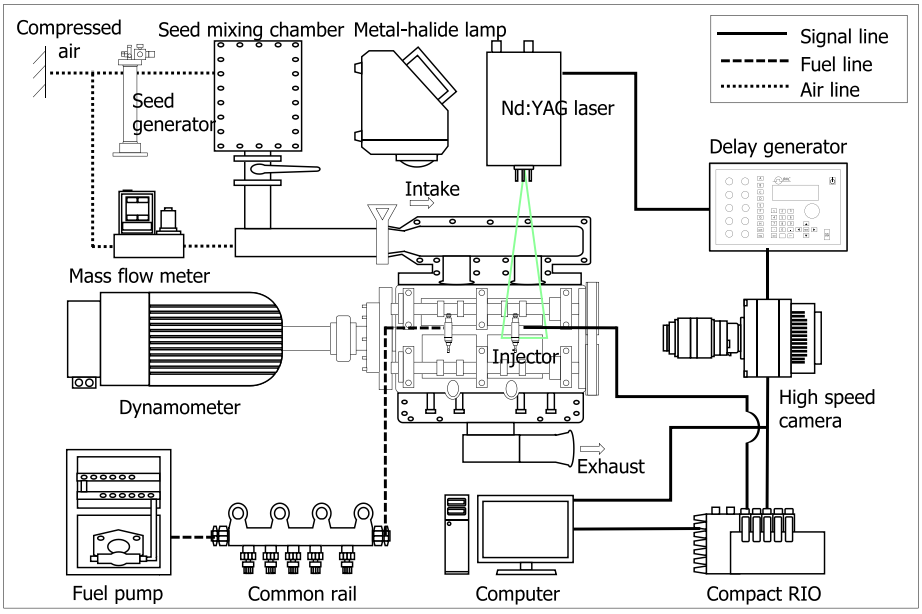

Fig. 3. Schematic of the optically accessible engine.

2. Experimental setup

2.1. Optically accessible engine

To study the evolution of the in-cylinder flow and spray structure in the engine cylinder, PIV measurements and the Mie-scattering imaging technique were implemented in a four-valve, 2-cylinder optically accessible engine. A four stroke cycle 2-cylinder engine with a pent-roof-shaped combustion chamber was used for this investigation. The optically accessible engine was fabricated as a 2-cylinder engine to reflect the interference between the cylinders. Both cylinders comprised transparent combustion chambers made of quartz; however, visualization of the in-cylinder flow was achieved in only one cylinder (Fig. 1). Furthermore, lubricant oil was not supplied to the combustion chamber because it could disturb the visualization of the in-cylinder flow. Consequently, Rulon was employed as a piston ring component to reduce the friction between the quartz cylinder wall and the piston ring. The connecting rod (con-rod) and piston crown were produced using aluminum to decrease the weight and inertial force, in an attempt to reduce the influence of the piston slap process. The optically accessible engine had a bore of 75.6 mm, stroke of 83.38 mm, displacement volume of 748.5 cc (2-cylinder), and compression ratio of 14:1. In addition, the intake and exhaust valves opened from bTDC 332° to bTDC 114° and aTDC 152° to aTDC 370°, respectively. Moreover, no valve overlap existed between the intake and exhaust valves. Detailed specifications of the optically accessible engine are listed in Table 1.

A high-pressure center-mounted solenoid-type injector was used as the test injector, which had seven holes and a nozzle hole diameter of

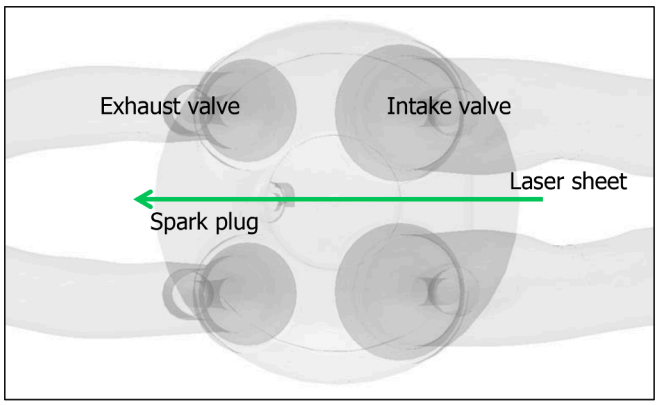

(a)

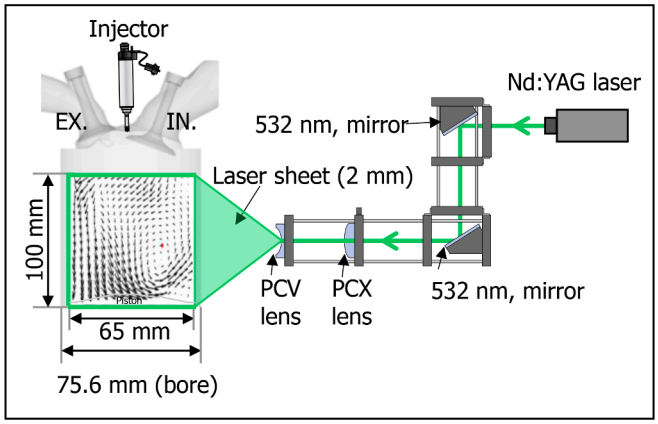

(b)

Fig. 4. Configuration of the PIV system: (a) location of the laser sheet and (b) configuration of the laser system.

Table 2
Specifications of the PIV system.

Items	Details
Camera	High-speed camera (Phantom, VEO 710L)
Laser	Nd:YAG pulse laser (26 mJ, double cavity)
Region of interest	65 × 100 mm
Resolution	320 × 344 pixels
Seed	10 μm, hollow sphere glass
PIV image time interval (dt)	Intake stroke:20 μs (@ 1500 rpm) Compression stroke:40 μs (@ 1500 rpm)
Interrogation area	32 × 32 pixels (50% overlap)
Correlation algorithm	Fast Fourier transform

100 μm along with a maximum injection pressure of 1,000 bar. Three plumes were developed toward the left side of the cylinder, which was the exhaust direction, considering the spark plug location, which was located between the exhaust valves. The spray structure and spark plug locations are depicted in Fig. 2.

A schematic of the optically accessible engine operating system is illustrated in Fig. 3. The intake air was supplied through a mass flow controller as well as an intake chamber that was used to reduce the fluctuation of the intake flow entering the manifold during engine operation. The intake air was seeded with hollow spherical glass particles (diameter: 10 μm) using a seed generator and a seed mixing chamber. Real-time engine operation data were acquired using the NI DAQ. Furthermore, the fuel injection and image capturing timings were controlled via an NI compact RIO and a delay generator with a TDC signal from an encoder attached directly to the crank shaft. The speed of the optically accessible engine was controlled by an AC motor and a motor controller. Moreover, the fuel was supplied to the test injectors through a fuel tank, fuel pump, and common rail.

2.2. Particle image velocimetry system

A schematic of the PIV system and the region of interest are depicted in Fig. 4. A laser beam was generated using an Nd:YAG laser with a double cavity, power of 26 mJ, and wavelength of 532 nm. The generated laser beam was reflected by a 45° mirror, which only reflected the 532 nm wavelength, and was expanded as a 2 mm laser sheet through planar convex and concave lenses. Thereafter, the laser sheet passed through the middle of the quartz cylinder from the intake to the exhaust valve, as shown in Fig. 4(a). The image plane had a width and height of 65 and 100 mm, respectively, except for the pent-roof region, as depicted in Fig. 4(b). The pent-roof region is an important part of the SI engine, but cannot be visualized owing to design limitations. Therefore, CFD was employed to confirm the characteristics of the in-cylinder flow and mixture formation in the pent-roof region. The illuminated particles were captured using a high-speed camera (Phantom, VEO 710L) having a Nikon 35 mm macro lens. The captured raw PIV images were processed using MATLAB software (PIV lab). Furthermore, additional functions, such as computing the tumble ratio, TKE, and tumble center position were included to quantitatively evaluate the in-cylinder flow. Data processing was performed by employing three processes. The details regarding the PIV image processing are provided in the research of Thielicke et al. [26]. The first process is image pre-processing. Regions with low and high exposures were optimized using a contrast limited adaptive histogram (CLAHE) algorithm, which increased the readability of image data. Subsequently, the background image was subtracted from the original PIV image using an intensity high-pass filter, which reduced the background noise. In addition, certain small regions of the image brightness intensity were adjusted using an intensity capping filter. The second process involved image evaluation. The particle displacement was detected using fast Fourier transform (FFT) cross-correlation coupled with a 2× 3-point algorithm. The FFT algorithm was employed to reduce the computational cost. In this study, the interrogation area contained 32 × 32 pixels (50% overlap). Finally, data validation, interpolation [27], and smoothing [28] were performed in the last process. The PIV lab software enabled semi-automatic data validation, while interpolation was performed using a boundary value solver and a penalized least-squares method was implemented to smoothen the PIV data. The details of the PIV system are presented in Table 2.

Exported data including velocity and position components obtained from the PIV lab were processed using a MATLAB image processing tool. The sequence for the image processing is shown in Fig. 5. The captured PIV raw image (Fig. 5(a)) was processed through the PIV lab to acquire an instantaneous flow field (Fig. 5(b)). The mean flow field (Fig. 5(c)) was computed using 60 instantaneous images in this study. Furthermore, the mean flow field was used as a representative in-cylinder flow at each crank angle.

2.3. Vector field computation

In a real engine, the in-cylinder flow exhibits a three-dimensional structure, such as tumble and swirl flow. However, a captured vertical image plane is two-dimensional; thus, the in-cylinder flow of the two-dimensional PIV system cannot fully reflect the in-cylinder flow of a real engine. Therefore, we focused on tumble flow because the primary motion of tumble flow is two-dimensional. The PIV data acquired from the two-dimensional system can be used to comprehend and analyze the characteristics of the bulk in-cylinder flow motion. We calculated the tumble ratio, TKE, and tumble center in the vertical plane. Moreover, we defined the flow rotation intensity to understand the structure of the in-cylinder flow.

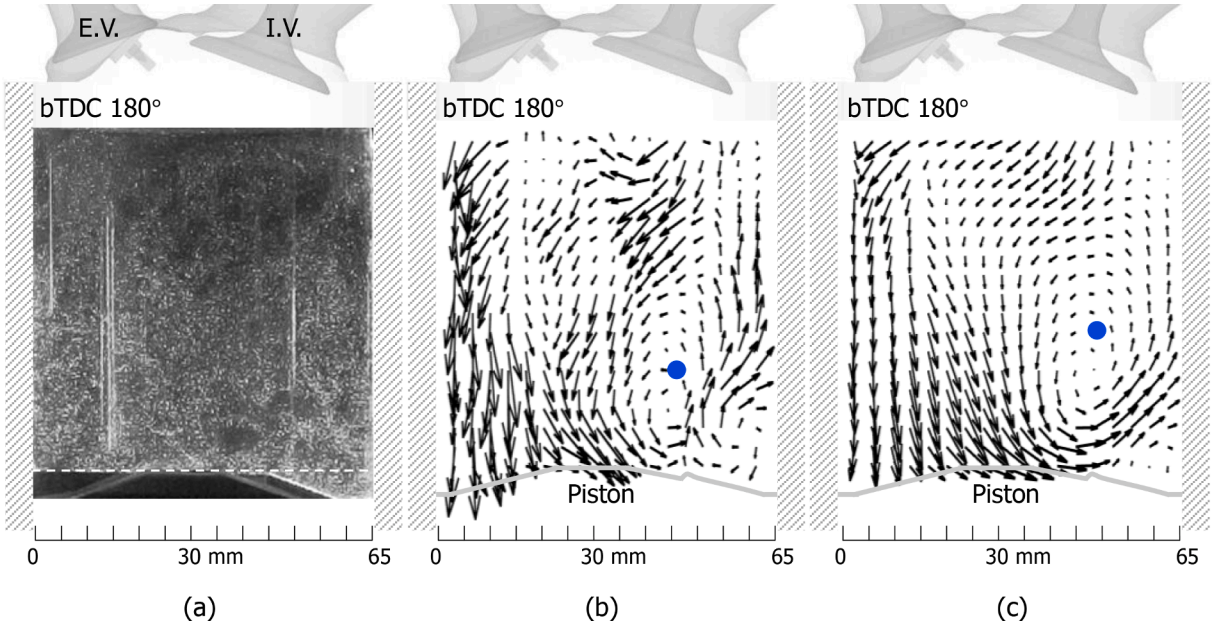

Fig. 5. PIV image processing: (a) PIV raw image, (b) an instantaneous image, and (c) a mean flow field.

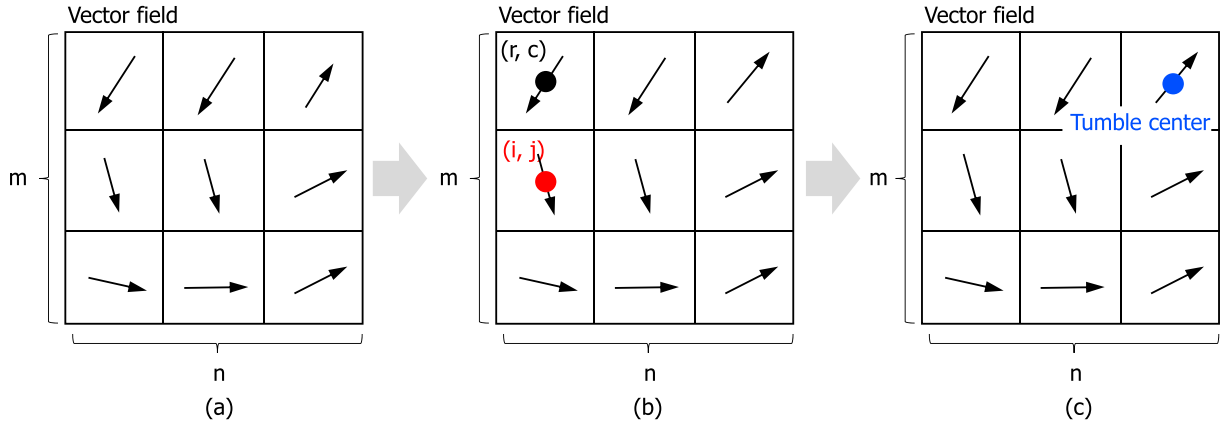

Fig. 6. Calculation of the tumble center: (a) m × n vector field, (b) calculation of the summation of a moment based on (r, c), and (c) determination of the location of the tumble center.

2.3.1. Tumble center

In this study, a tumble center was defined as the position having maximum moment summation, as shown in Fig. 6. An alternative definition for a vortex center can be found in [29]. One or more positions can be employed as a vortex center. In contrast, the tumble center defined in this study has a high probability of being in one position, except for the case wherein the in-cylinder flow is completely symmetrical. Following the definition of a tumble center, the in-cylinder flow rotates the strongest based on the tumble center. Moment summation (MS) was calculated using the following equation:

$$\mathrm{MS} = \sum_{i=1}^{n}\sum_{j=1}^{m}((\vec{r}_{i,j} - \vec{r}_{r,c}) \times \vec{V}_{i,j}) \tag{1}$$

where (r, c) is a position in vector field.

2.3.2. Tumble ratio

In the research conducted by Salazar et al., tumble ratio was defined as the ratio of the angular velocity of the in-cylinder flow based on the combustion-chamber center, including the pent-roof region, to the angular velocity of an engine [30]. However, in this study, the angular velocity of the in-cylinder flow was calculated based on the tumble center matching the definition of the tumble ratio experimentally and the definition of the tumble ratio in CFD. The equation used to calculate the tumble ratio (TR) is as follows:

$$\mathrm{TR} = \frac{\sum_{i=1}^{n}\sum_{j=1}^{m}(\vec{r}_{i,j} - \vec{r}_{tc}) \times \vec{V}_{i,j}}{\omega\sum_{i=1}^{n}\sum_{j=1}^{m}(\vec{r}_{i,j} - \vec{r}_{tc})\cdot(\vec{r}_{i,j} - \vec{r}_{tc})} \tag{2}$$

where $(\vec{r}_{i,j} - \vec{r}_{tc})$ is the distance of a particular location with indices (i,j) from the center of the rotation, $\vec{V}_{i,j}$ is the velocity at that location, and ω

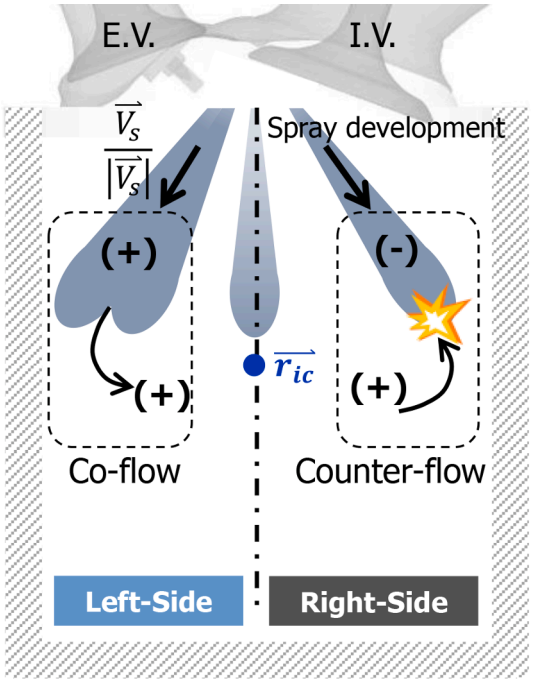

Fig. 7. Definitions of the spray and in-cylinder flow directions.

Table 3
Specifications of the experimental conditions.

Items	Details
Applied visualization techniques	PIV and Mie-scattering
Fuel	gasoline
Engine speed (rpm)	1500
Intake pressure (bar)	1.0 (wide-open throttle)
Injection pressure (bar)	700
Energizing duration (ms)	2.6
Injection timing (bTDC°)	300, 270, 240, 210, 180, 150, 120, 90, 60
Intake air temperature (°C)	35
Fuel temperature (°C)	90

is the angular (crank) speed of the engine. The tumble ratio represents the ratio of the angular velocity of the flow to the angular velocity of the engine rotation. Therefore, the intensity and direction of flow rotation in the combustion chamber can be determined. In this study, r_{tc} was selected as the tumble center.

2.3.3. Turbulent kinetic energy

TKE was calculated using the following equation:

$$\mathrm{TKE} = 0.5 \times \left(\overline{(u')^2} + \overline{(v')^2}\right) \tag{3}$$

where u' and v' are the total radial and axial velocities of a turbulent vector field in an image plane, respectively. The turbulent flow field can be derived by subtracting the mean flow field from the instantaneous flow field. As mentioned earlier, in this study, the mean flow field was derived from 60 instantaneous PIV images.

2.3.4. Flow rotation intensity

A counterclockwise rotation was selected as the positive direction, as depicted in Fig. 7. Therefore, the spray development direction is positive on the left side of the cylinder, and negative on the right side. Co-flow is defined as a flow that is in the same direction as that of the spray development and in-cylinder flow, whereas counter-flow is an in-cylinder flow that is in the opposite direction of the spray development. In other words, the momentums of the spray and in-cylinder flow

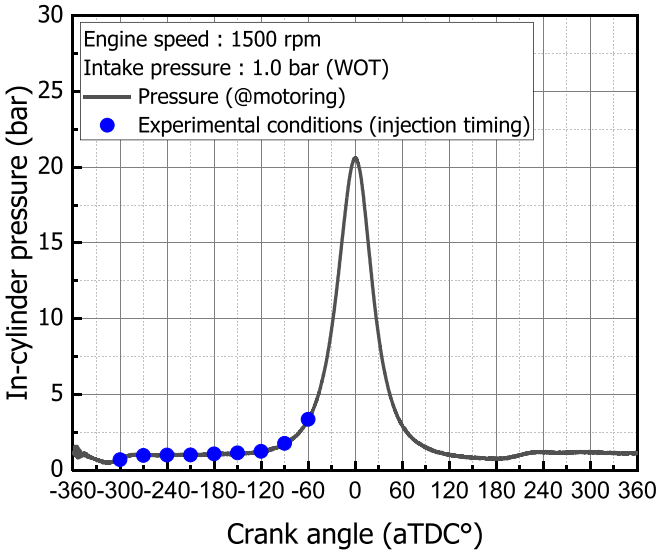

Fig. 8. In-cylinder pressure profile with experimental conditions (@ 1,500 rpm, NA, motoring).

are lost owing to the collision with each other when the directions of the spray and in-cylinder flow are different. The flow rotation intensity was calculated by separating the image plane into the left and right sides to understand the interaction between the spray development and in-cylinder flow. To quantitatively analyze the co-flow and counter-flow depending on the crank angle, the flow rotation intensity is defined as follows:

$$D_s = \frac{\vec{V}_s}{\left|\vec{V}_s\right|} \tag{4}$$

$$TR_i = \frac{\sum_{i=1}^{n}\sum_{j=1}^{m}(\vec{r}_{i,j} - \vec{r}_{ic}) \times \vec{V}_{i,j}}{\omega\sum_{i=1}^{n}\sum_{j=1}^{m}(\vec{r}_{i,j} - \vec{r}_{ic})\bullet(\vec{r}_{i,j} - \vec{r}_{ic})} \tag{5}$$

where D_s is direction of spray development, and TR_i is tumble ratio based on the image center.

Flow rotation intensity = (direction of spray development) • (tumble ratio based on image center)

$$= \frac{\vec{V}_s}{\left|\vec{V}_s\right|}\bullet\frac{\sum_{i=1}^{n}\sum_{j=1}^{m}(\vec{r}_{i,j} - \vec{r}_{ic}) \times \vec{V}_{i,j}}{\omega\sum_{i=1}^{n}\sum_{j=1}^{m}(\vec{r}_{i,j} - \vec{r}_{ic})\bullet(\vec{r}_{i,j} - \vec{r}_{ic})} \tag{6}$$

where $\frac{\vec{V}_s}{|\vec{V}_s|}$ is a unit vector that represents the direction of the spray development. The tumble ratio based on the image center is the similar in definition to the tumble ratio, except for $\vec{r}_{ic}$, which is the image center. Further, the flow rotation intensity is defined as the inner product of the direction of spray development and tumble ratio based on the image center. As in Fig. 7, the flow rotation intensity has a positive value on the left side. However, although the right side flow is in the same direction as the left side flow, the flow rotation intensity on the right side is negative. This is because the direction of the spray development is in the negative direction. Thus, the presence of co-flow or counter-flow is determined based on the sign of the flow rotation intensity. For a positive value, the flow is a co-flow.

2.4. Experimental conditions

In this study, two types of imaging techniques were applied to visualize the in-cylinder flow and spray structure. A PIV imaging

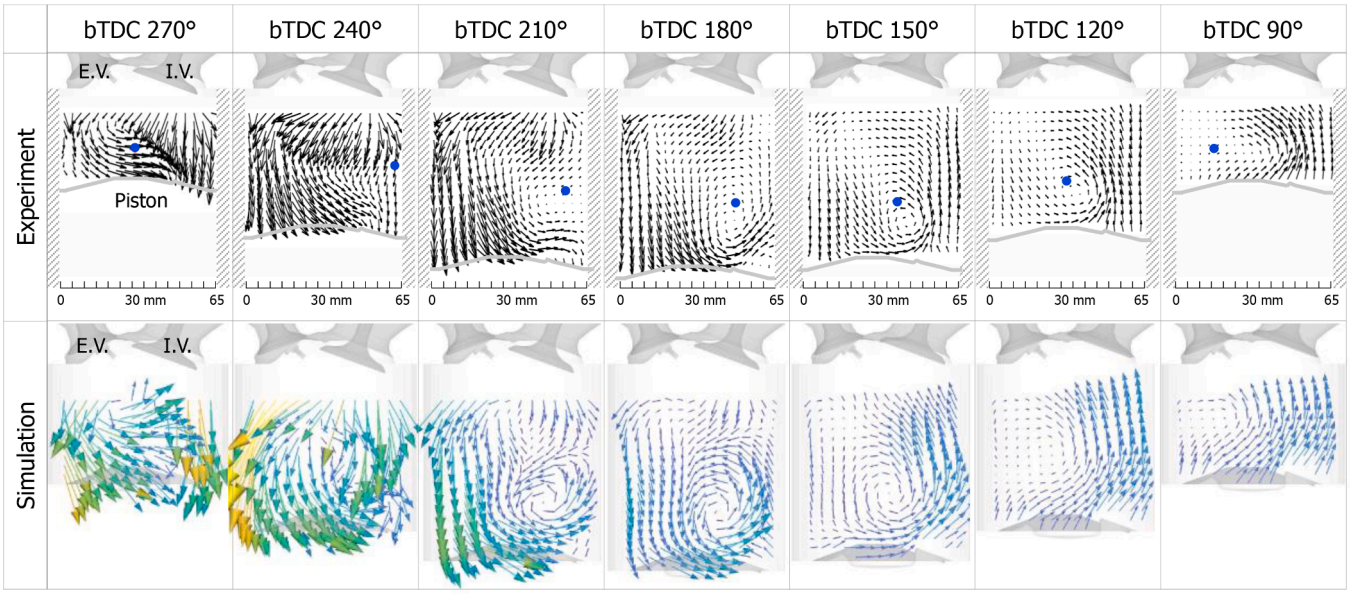

Fig. 9. In-cylinder flow field validation (@ 1,500 rpm, NA, w/o injection).

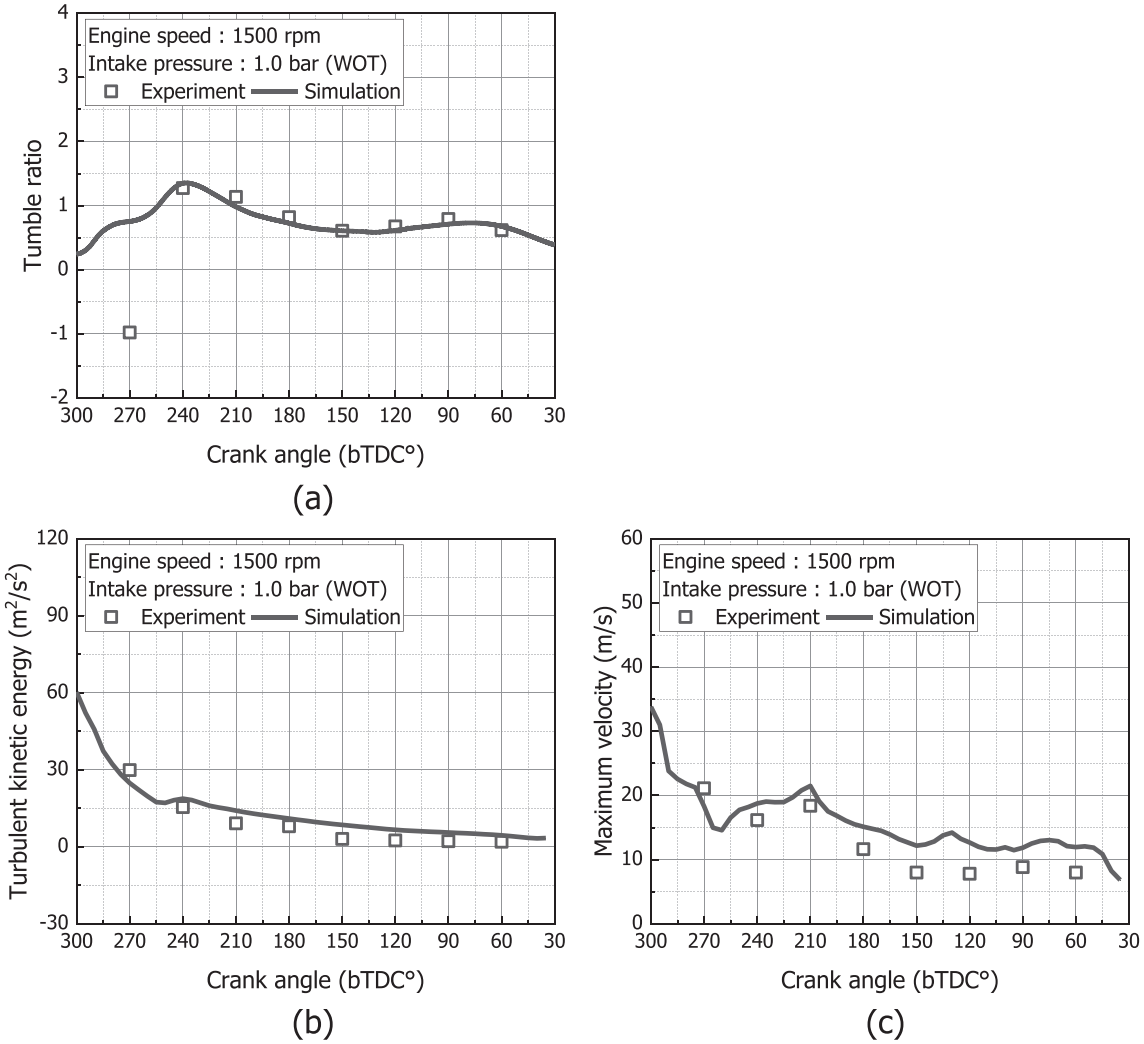

Fig. 10. Quantitative indices validation: (a) tumble ratio, (b) TKE, and (c) maximum velocity.

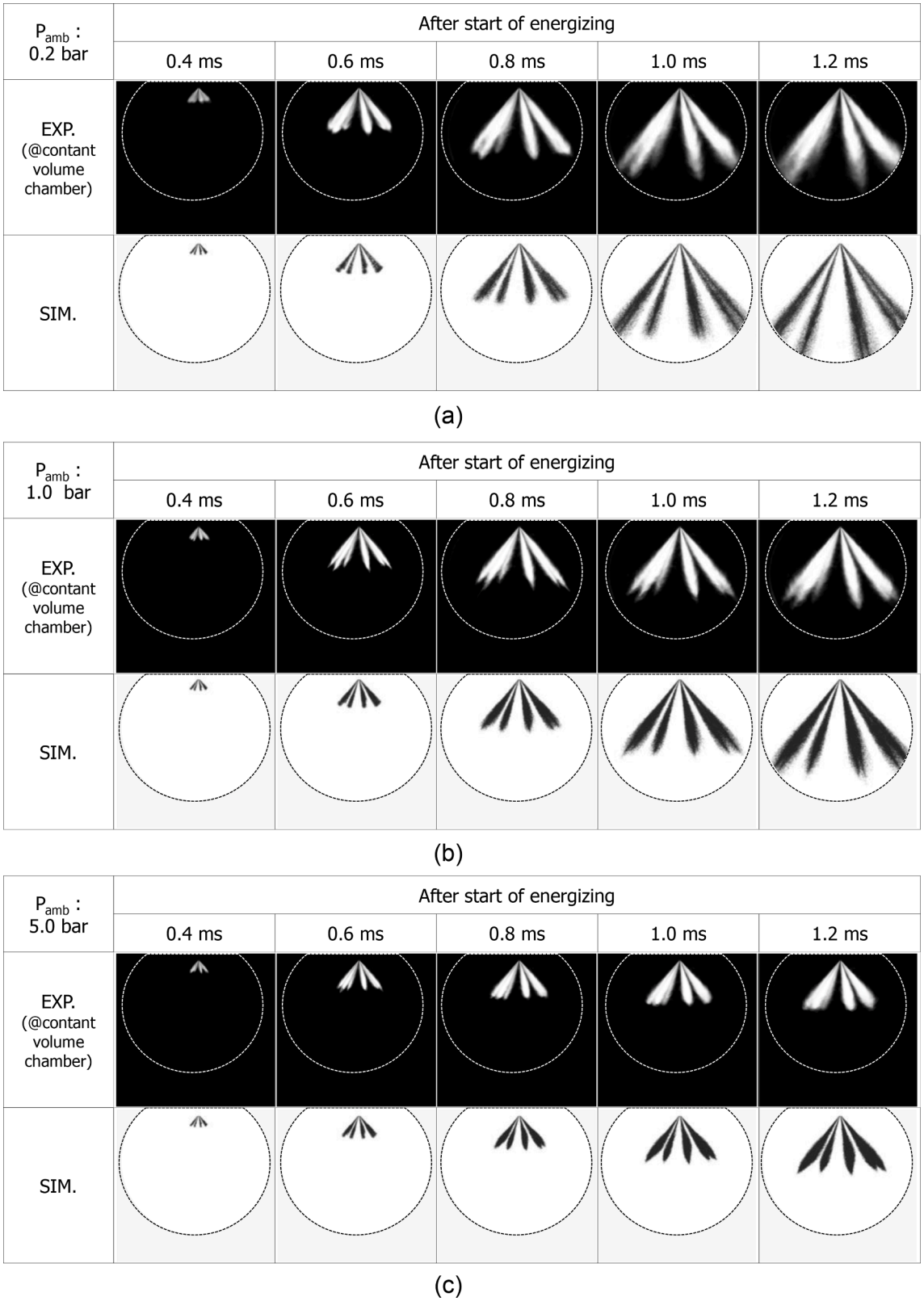

Fig. 11. Spray structure validation at an injection pressure of 700 bar and ambient pressures of (a) 0.2 bar, (b) 1.0 bar, and (c) 5.0 bar.

technique was used to visualize the in-cylinder flow, wherein the image capturing timing was varied from bTDC 270° to bTDC 60° with an interval of 30° at 1,500 rpm. For the entirety of the experiment, the intake manifold pressure was maintained at 1.0 bar in the naturally aspirated (NA) condition with a wide-open throttle (WOT). Furthermore, to analyze the effects of fuel injection on the in-cylinder flow, the fuel was injected at an injection pressure of 700 bar under different injection timings. To observe the effects of in-cylinder flow on the spray structure, spray images were captured using the Mie-scattering technique depending on the injection timing. Detailed experimental conditions are listed in Table 3.

Fig. 8 depicts the in-cylinder pressure for various injection timing

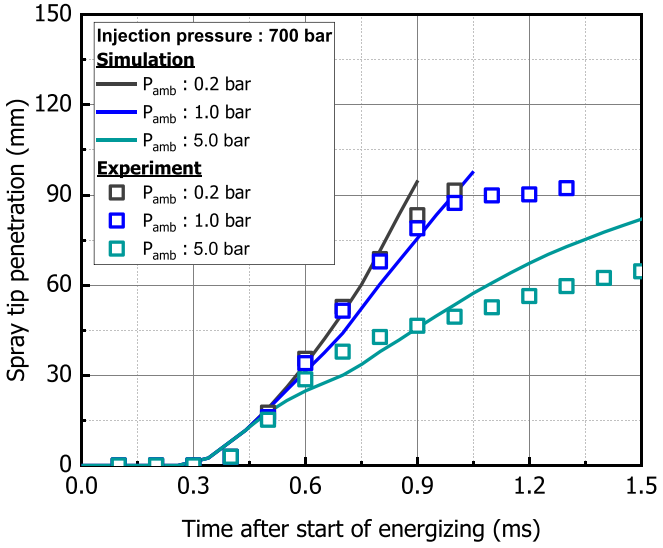

Fig. 12. Spray tip penetration validation at an injection pressure of 700 bar.

Table 4
Spray break-up model constants.

Items	Details
KH model size constant	0.61
KH model velocity constant	0.188
KH model break-up time constant	100
RT model size constant	0.1
RT model break-up length constant	0.0
RT model break-up time constant	1.0

experimental conditions. The fuel was injected from bTDC 300° to bTDC 90°, and correspondingly, the in-cylinder pressure increased from 0.7 to 3.4 bar. In this study, the spray structure depending on the injection timing was analyzed by considering the ambient pressure and in-cylinder flow.

3. Computational methodology

3.1. Simulation model

In this study, CONVERGE v2.4 was used as a CFD program for engine simulations, and the RNG k-ε model was employed to achieve closure in the turbulence model. For spray modeling, the KH-RT model, which is appropriate for predicting the spray atomization process for high injection pressures, was used [31]. In addition, isooctane was used to simulate the gasoline spray development and atomization processes.

3.2. Model validation

The model was verified by considering quantitative and qualitative aspects based on a comparison of the experimental and simulation results. The engine simulation results were compared with the PIV experiments under the same operating conditions. As shown in Fig. 9, the velocity distribution and vortex core location in the PIV results are consistent with the simulation results. Furthermore, for a quantitative perspective, the tumble ratio was compared, as shown in Fig. 10(a). The tumble ratio in the simulation was calculated based on the tumble center in the cylinder region. Except for the tumble ratio in bTDC 270° where strong turbulence was induced by high intake velocity, the tumbler ratio ensured consistency between the experiment and simulation with an error ranging from a minimum of 0.1% (at bTDC 150°) to a maximum of 13.5% (at bTDC 210°). In addition, the simulation results of the TKE and maximum velocity in the same region of the PIV experiment were compared with those of the experiments (Fig. 10(b) and 10(c)). TKE exhibited a maximum and minimum of 5.5 and 2.5 m^2/s^2, respectively. Thus, both the simulation results of the TKE and maximum velocity exhibited a trend similar to that of the experiment.

Spray model validation was conducted through a break-up constant adjustment, wherein isooctane was selected as the working fluid. The results of the validation are shown in Figs. 11 and 12. The simulation results of the spray structure obtained with different ambient pressures are consistent with the experimental results (Fig. 11). The spray tip penetration was consistent for ambient pressures of 0.2 and 1.0 bar. In contrast, for an ambient pressure of 5.0 bar, the simulation result shows slower spray development, that is, 0.9 ms later than the experiment result. However, considering the different ambient pressures, the overall trend was consistent between the experimental and simulation results. The final model constants are presented in Table 4.

4. Results and discussion

In this study, the in-cylinder flow was visualized using PIV measurements depending on the crank angle. The in-cylinder flow data are useful for comprehending the overall structure of the in-cylinder flow. In addition, the fuel was injected at various injection timings to analyze the effects of fuel injection on the in-cylinder flow. Consequently, using the Mie-scattering imaging technique, the spray development was visualized under different injection timings to investigate the effects of in-cylinder flow on the spray structure. However, the in-cylinder flow field in the pent-roof region, which cannot be visualized in the experiments owing to design limitations, was analyzed using CFD. In addition, the mixture formation process, depending on the injection timing, was investigated.

4.1. Characteristics of mean in-cylinder flow without fuel injection

Fig. 13 depicts the mean in-cylinder flow field depending on the crank angle at an engine speed of 1,500 rpm. In the early stage of the intake stroke at bTDC 270°, air flowed into the left and right sides of the cylinder. Subsequently, the left side intake flow collided with the piston head, resulting in the intake flow losing momentum. As the right side intake flow was supplied directly following the surface of the liner, the clockwise in-cylinder flow with a high velocity was stronger than the counterclockwise in-cylinder flow at bTDC 270°. Following the piston descent, a tumble flow with counterclockwise rotation was formed. Subsequently, during the intake stroke, the in-cylinder flow on the left side was stronger than the in-cylinder flow on the right side owing to the flow of the intake air from right to left. However, when the intake valves were closed and the piston ascended, the high momentum of the left side moved toward the right side. Consequently, the main tumble motion in the compression stroke occurred on the right side. However, the high momentum supplied at the initial stage of the intake stroke cannot be maintained because the momentum is dissipated by the friction loss and shear force, which is caused by the relative velocity between the inflowing air and existing in-cylinder air [32,33]. Therefore, the mean velocity of the in-cylinder flow continuously decreased from the intake stroke to the compression stroke, as shown in Fig. 14. Although there was a continuous decrease in velocity, the maximum velocity was maintained at a higher value than the piston speed during the intake and compression strokes. In contrast, the mean velocity was lower than the piston speed after bTDC 150°. This is because there was no additional source to supply momentum except for the piston movement and the in-cylinder pressure increased during the compression stroke.

The tumble ratio, which depends on the crank angle, is shown in Fig. 15. The results of the tumble ratio demonstrated the same tendency as that of the in-cylinder flow visualization results. At bTDC 270°, the in-cylinder flow rotated in the clockwise direction, resulting in the tumble ratio attaining a negative value. The tumble ratio decreased until bTDC

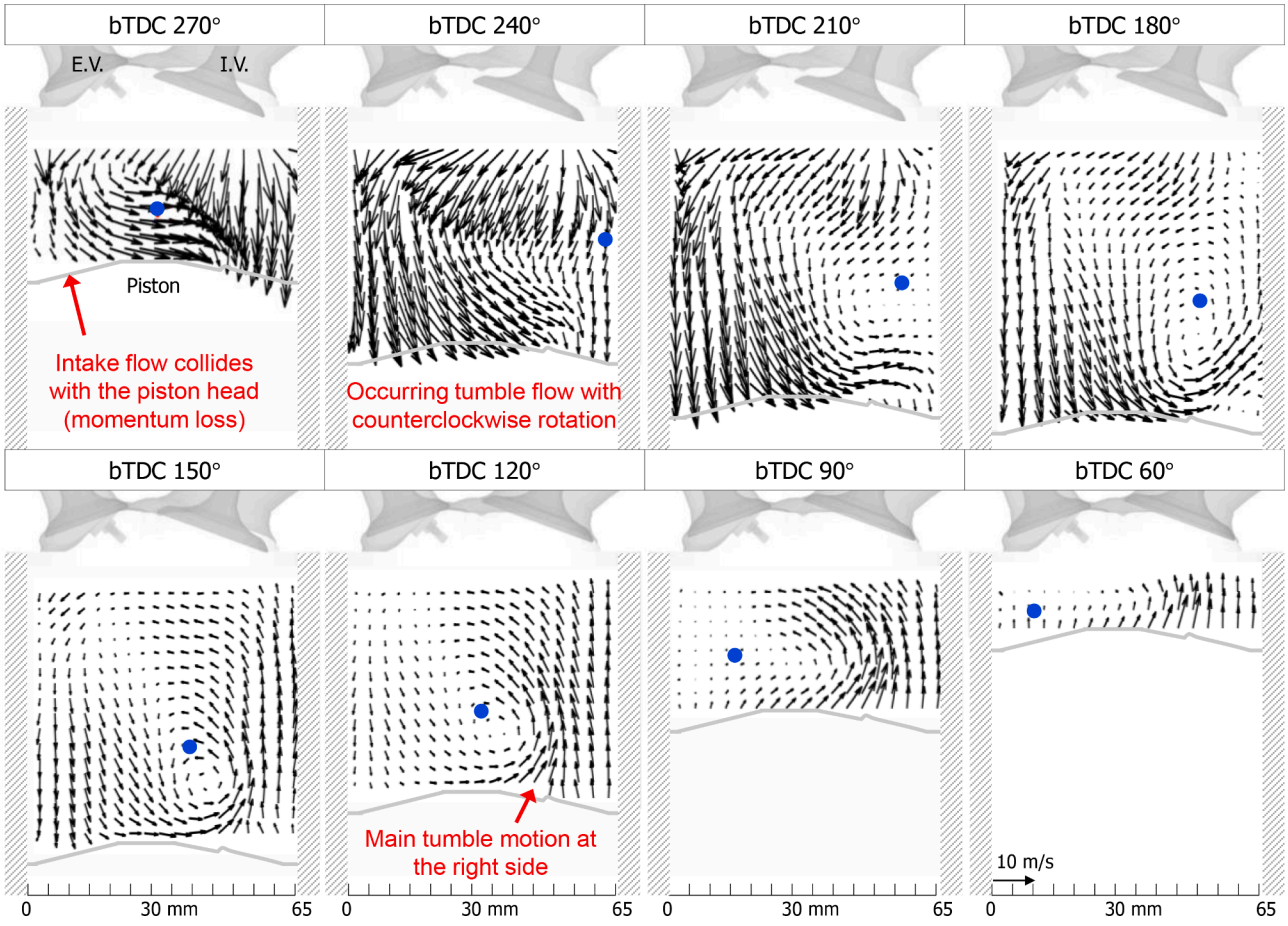

Fig. 13. Time series of mean in-cylinder flow field (@ 1,500 rpm, NA, w/o injection).

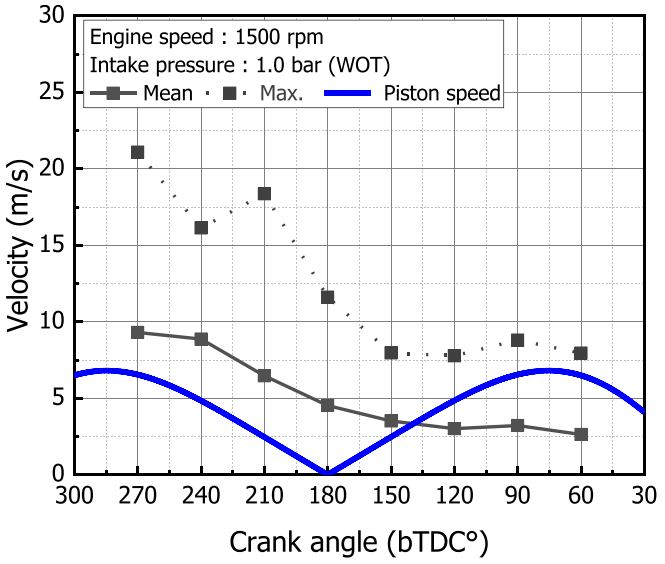

Fig. 14. In-cylinder flow velocity with piston speed (@ 1,500 rpm, NA, w/o injection).

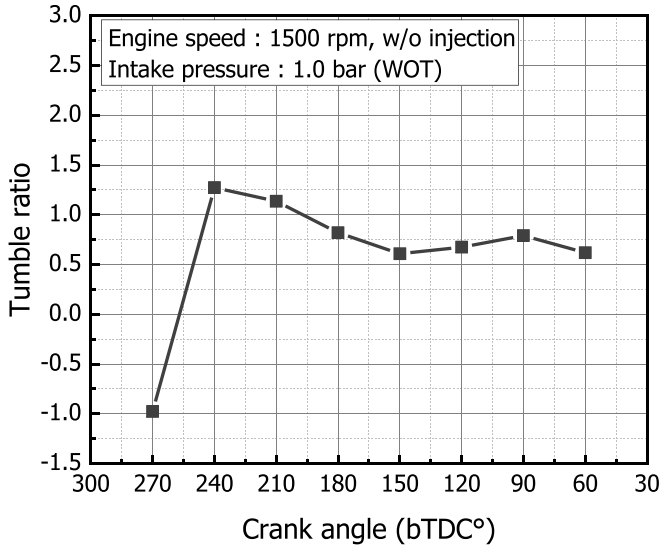

Fig. 15. Tumble ratio (@ 1,500 rpm, NA, w/o injection).

150° and thereafter increased slightly because the in-cylinder flow was intensified slightly by the ascending piston.

In addition, the TKE decreased continuously during the compression stroke because of the dissipation of momentum, as shown in Fig. 16. The maximum value of the TKE was attained at bTDC 270°, where the in-cylinder flow velocity was at its maximum. After bTDC 150°, the in-cylinder flow exhibited a weak flow, with a flow velocity lesser than the piston speed, resulting in the low velocity of the turbulent components. Therefore, the TKE converged to a similar level after bTDC 150°.

In this study, the characteristics of in-cylinder flow were analyzed by calculating the flow rotation intensity, which represents the in-cylinder

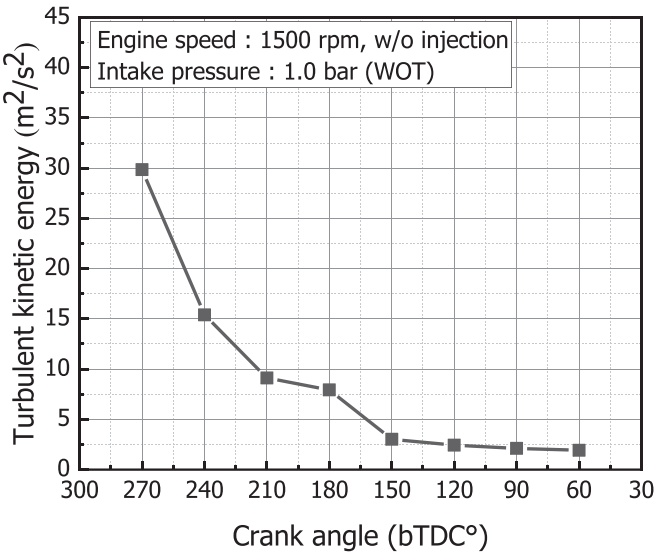

Fig. 16. TKE (@ 1,500 rpm, NA, w/o injection).

flow rotation intensity and direction, considering the direction of spray development. The flow rotation intensity was calculated separately for the left and right sides. Counter-flow, which has a direction opposite to that of the spray development, represents a flow rotation intensity below zero. Fig. 17 depicts the results of the flow rotation intensity depending on the crank angle. Here, the intensity of co-flow or counter-flow is expressed as a number with a positive or negative symbol for intuitive comprehension. For example, the absolute values of the flow rotation intensity in the range of 0–1 are expressed as (+) or (-). We separated the regions depending on the characteristics of the in-cylinder flow. In region 1, a strong co-flow expressed by the (+++) symbol occurred on the right side. In this region, the spray atomization performance can be increased owing to the interactions between the in-cylinder flow and spray [34,35]. This is because intake air with a high momentum flows in the cylinder, and the air collides with the spray. Moreover, there is a relatively long time to mix fuel and air until the spark timing; thus, the possibility of forming a homogeneous mixture around the spark timing increases [36,37]. A relatively weaker co-flow occurred in region 2 compared to that in region 1. The co-flow was still the dominant flow within the cylinder, particularly in the left side plane. However, the flow rotation intensity decreased compared to that in region 1 owing to the downward motion of the piston in region 2. This is because the suction force generated by the piston movement decreased, and correspondingly, the initial velocity of the intake air decreased owing to the increase in the inlet area. In the case of region 3, the counter-flow was stronger than the co-flow in the cylinder and moved in a direction opposite to that of the spray development. Therefore, it is difficult for the in-cylinder flow to carry fuel around the spark plug after the end of injection. Furthermore, region 3 represents the compression stroke that increases the in-cylinder pressure, thereby increasing the possibility of forming a stagnant fuel region [38,39]. Therefore, the division of regions in such a manner is useful for comprehending the mixture formation process and spray structure depending on the injection timing, because the injected fuel travels owing to its interaction with the in-cylinder flow.

Among the important factors for stable combustion is the in-cylinder flow of the pent-roof region, which cannot be visualized by PIV experiments owing to design limitations. Therefore, CFD was performed to understand the overall in-cylinder flow, particularly the in-cylinder flow of the pent-roof region near the TDC.

Fig. 18 depicts the CFD results for the in-cylinder flow depending on the crank angle. The in-cylinder flow exhibited a tendency similar to that of the experimental results. In the CFD results, strong co-flow occurred at bTDC 300° on the right side, while counter-flow occurred on the left side because the intake air collided with the piston head.

4.2. *Characteristics of mean in-cylinder flow with fuel injection and spray structure*

In this section, the characteristics of the in-cylinder flow and spray structure, depending on the injection timing, are studied. Fig. 19 depicts the spray development depending on the crank angle after the start of the injection. In the case of injecting fuel in region 1, the spray was scattered more prominently compared to that under other conditions. Moreover, the interaction between the plumes increased because of the collision of the spray with the strong intake air. Therefore, the boundary between the plumes was unclear [40]. In region 3, the in-cylinder flow was a weak counter-tumble, and the in-cylinder pressure was slightly higher than the atmospheric pressure. The spray developed directly and maintained the spray targeting location. Thus, an obvious separation between the plumes with a thin plume width was observed. In general, the plume width increased under high ambient pressure conditions owing to the increase in drag force [41–43]. However, in the case of

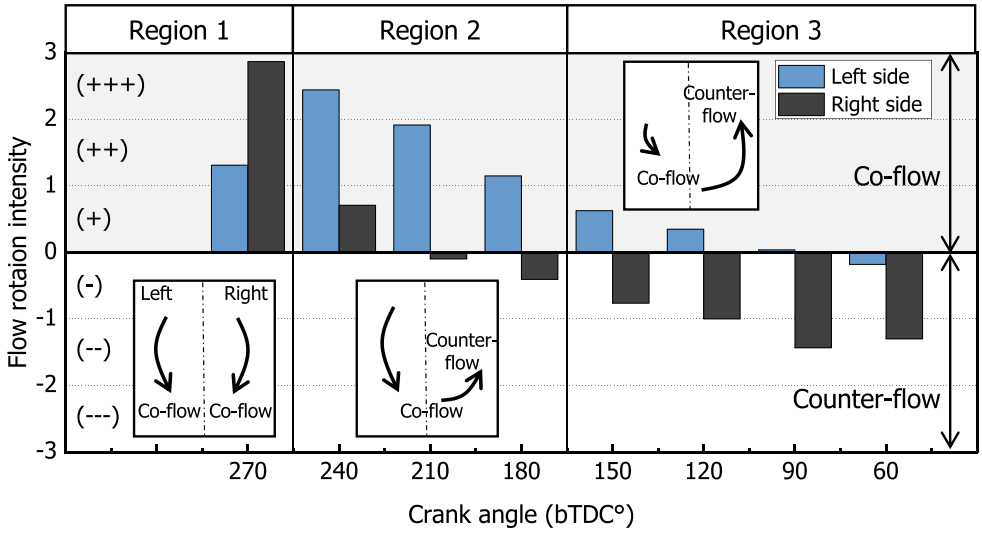

Fig. 17. Flow rotation intensity (@ 1,500 rpm, w/o injection).

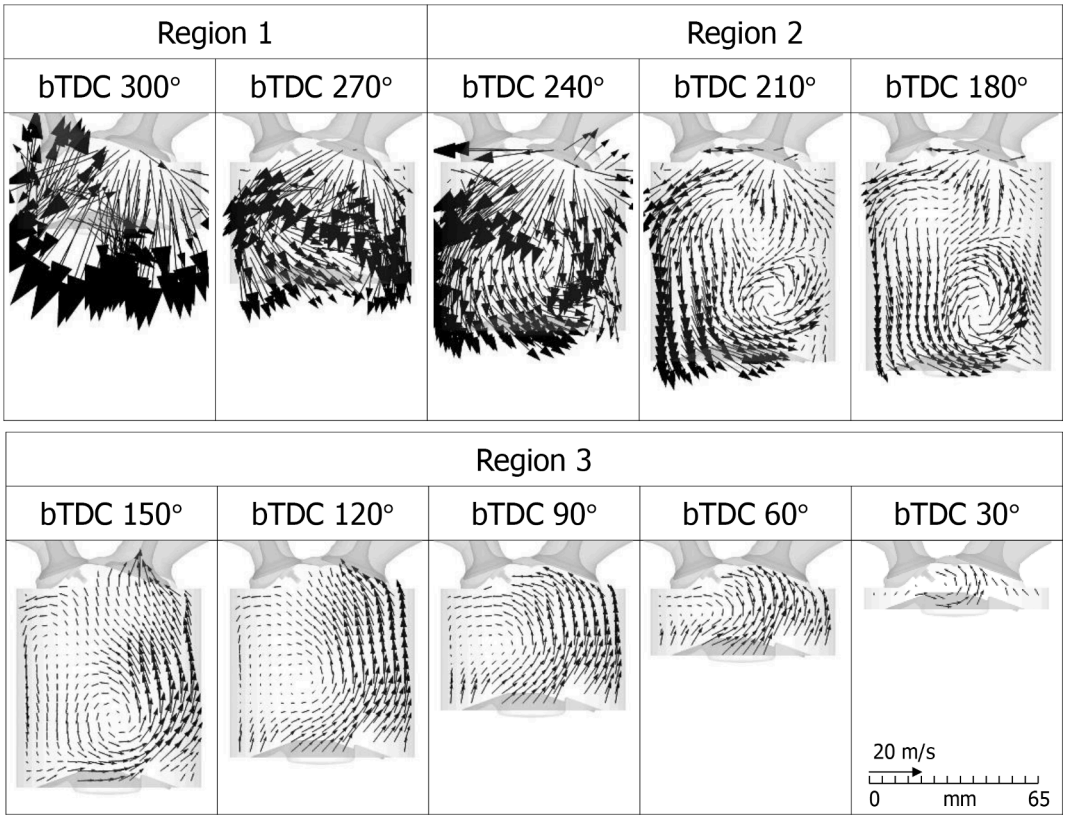

Fig. 18. CFD results of in-cylinder flow depending on crank angle (@ 1,500 rpm, w/o injection).

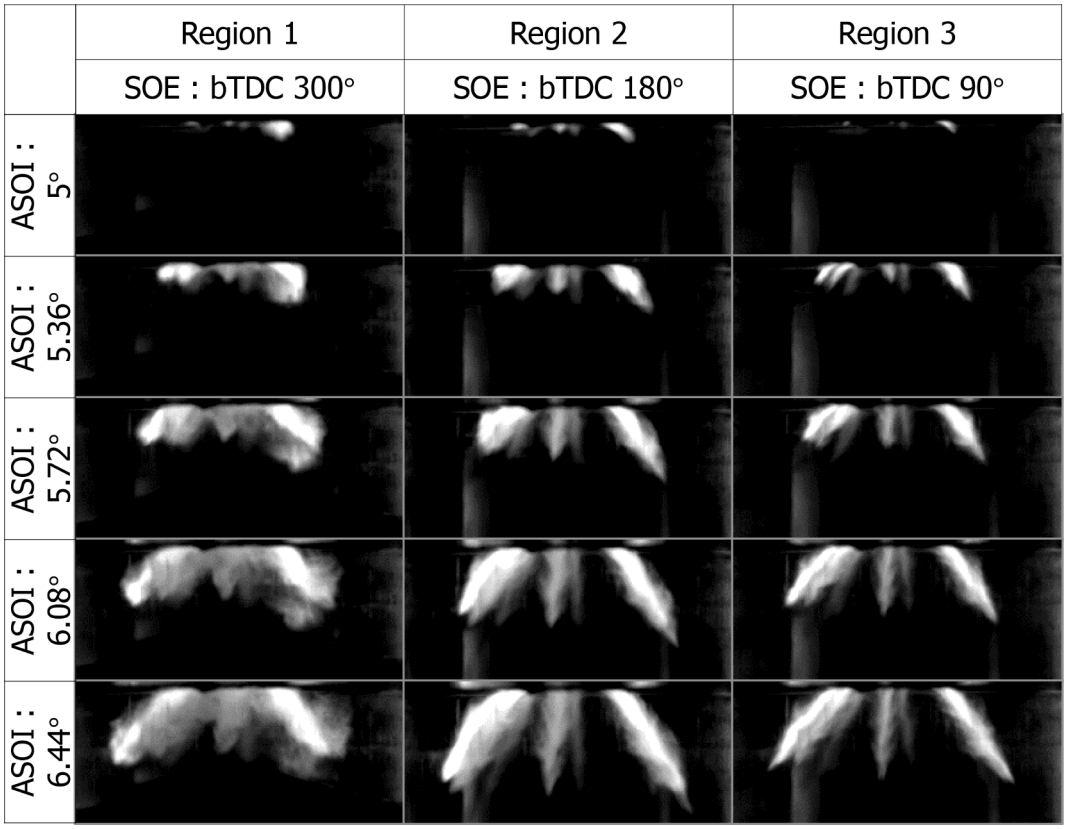

Fig. 19. Spray development depending on injection timing (@ 1,500 rpm, NA, P_{inj} : 700 bar).

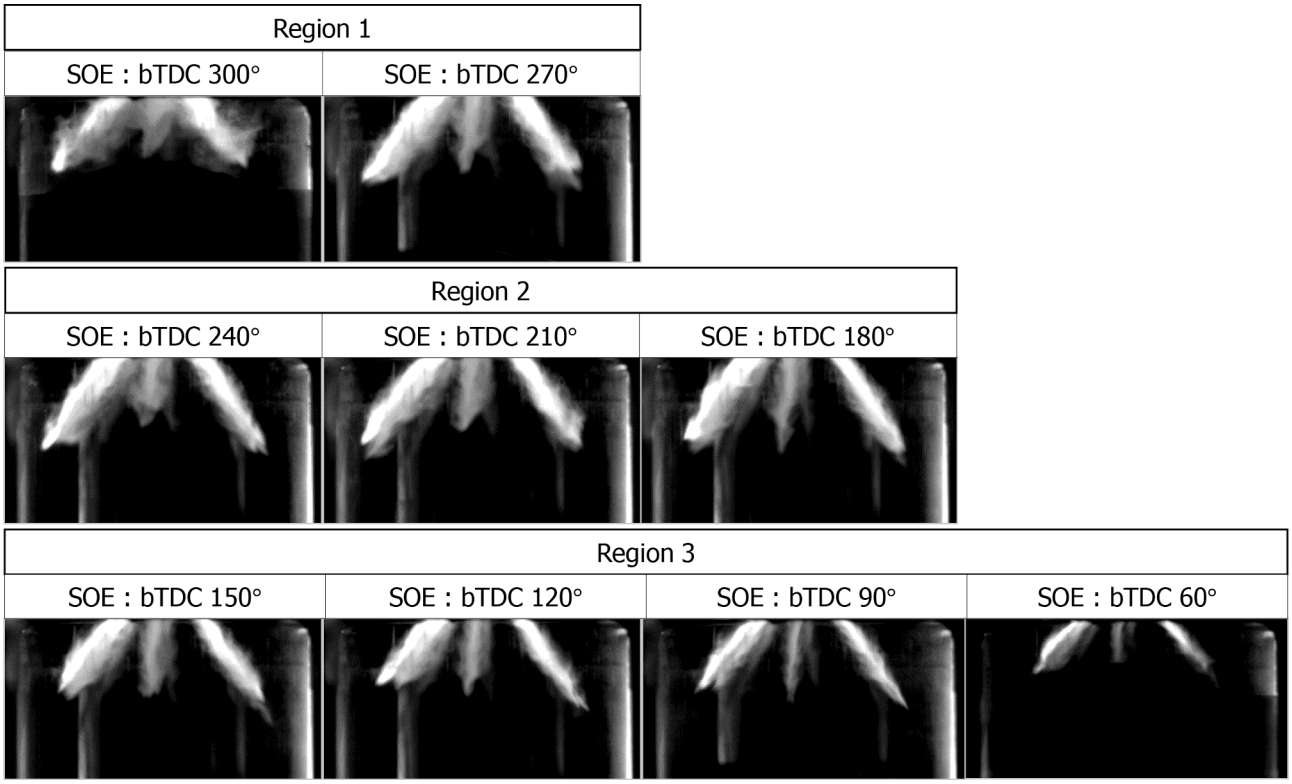

Fig. 20. Spray structure depending on injection timing (@ 1,500 rpm, NA, P_{inj}:700 bar).

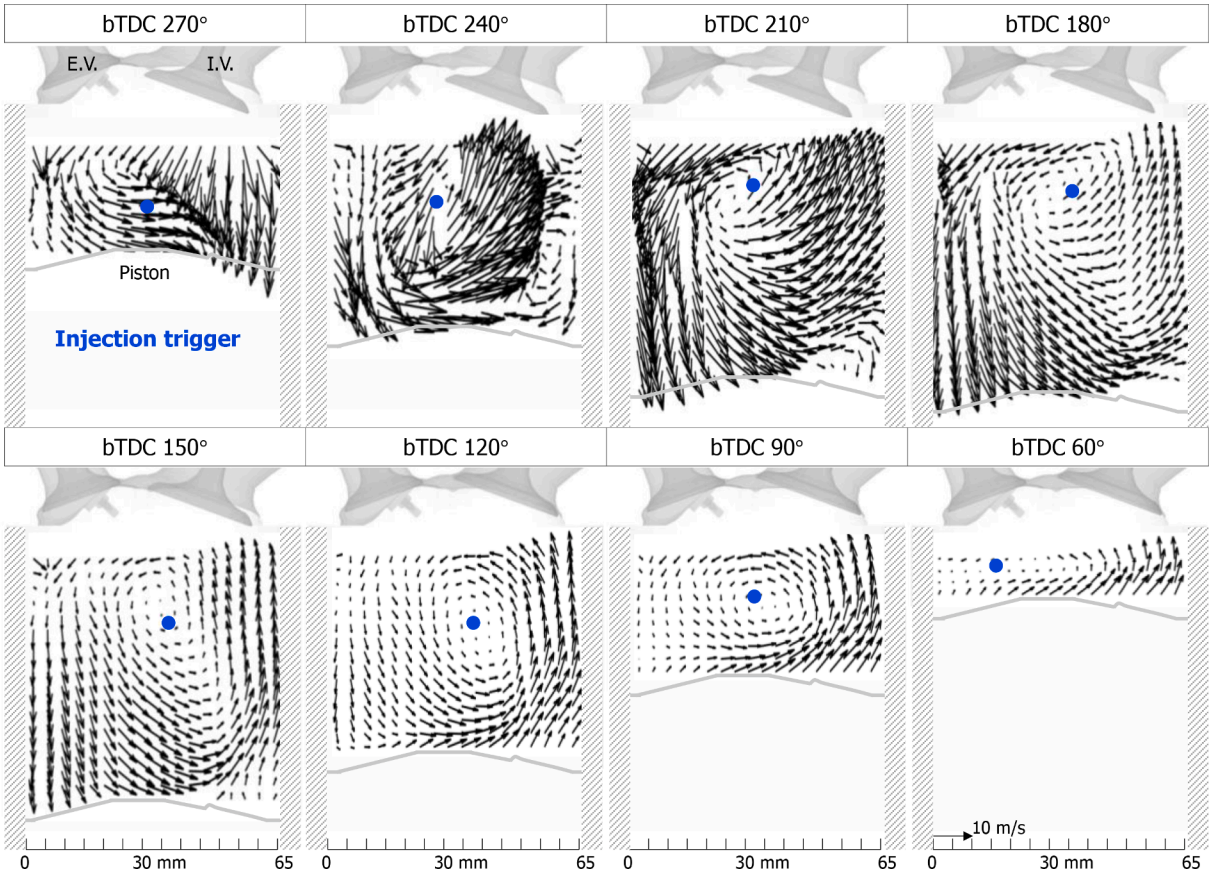

Fig. 21. Time series of mean in-cylinder flow field with injection (@ 1,500 rpm, NA, P_{inj}:700 bar, SOE:bTDC 270°).

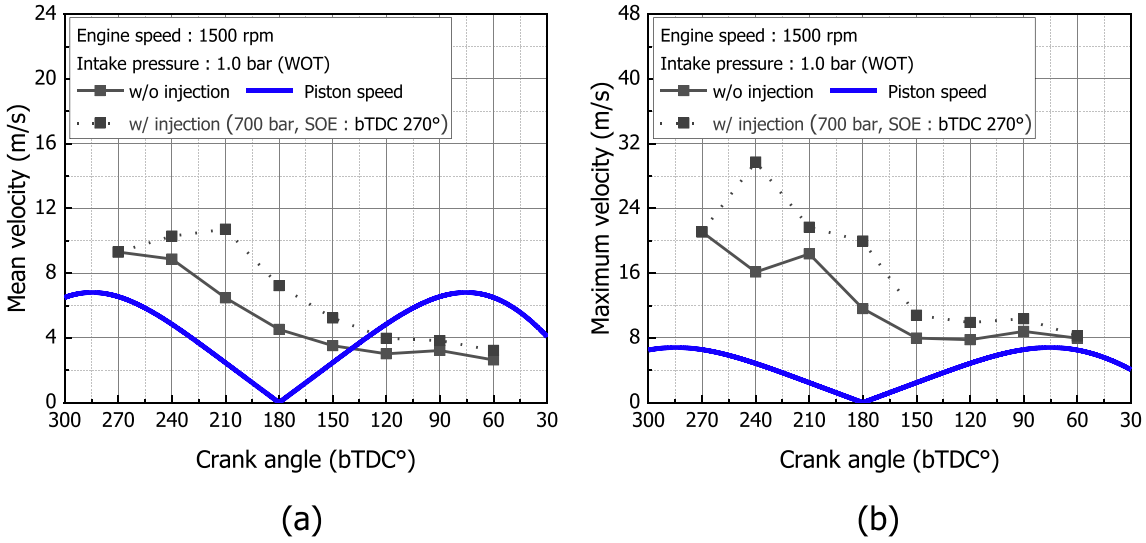

Fig. 22. Comparison of in-cylinder flow velocity depending on fuel injection: (a) mean velocity and (b) maximum velocity.

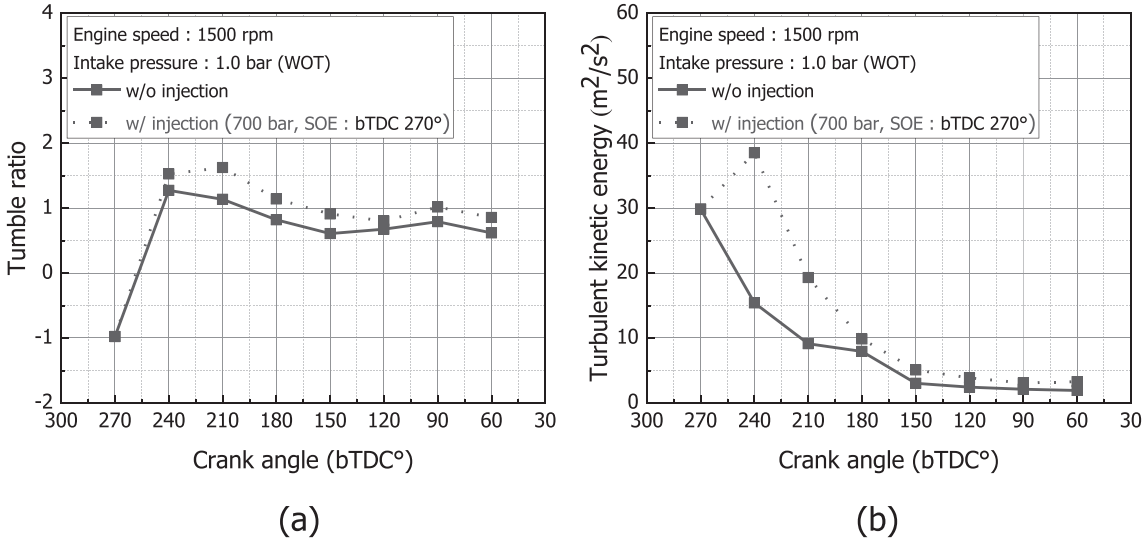

Fig. 23. Comparison of tumble ratio and TKE depending on fuel injection: (a) tumble ratio and (b) TKE.

regions 1 and 2, the plume was wider than the plume in region3 having a relatively high in-cylinder pressure. This is because the effects of the in-cylinder flow are larger than the effects of the drag force caused by the high ambient pressure.

The results of the spray structure depending on the injection timing are depicted in Fig. 20. In regions 1 and 2, the spray structure exhibited similar shapes except for bTDC 300° even with a difference in the co-flow intensity. This is because the intake flow does not possess sufficient momentum to cause a complete collapse of the spray structure, and the momentum of the spray is relatively high compared to the in-cylinder flow. The spray at bTDC 300° was scattered compared to that under the other conditions; however, spray targeting was still maintained. In the compression stroke, the counter-flow was intensified, and the in-cylinder pressure increased. The in-cylinder flow moving upward may disturb the spray development because the directions of spray development and in-cylinder flow are opposite to each other. However, the intensity of the counter-flow during the compression stroke was low; thus, the spray structure did not collapse.

The fuel was injected at an injection pressure of 700 bar at bTDC 270°, as shown in Fig. 21. The in-cylinder flow was intensified during the intake and compression strokes owing to fuel injection. This could be attributed to the additional energy that was supplied by fuel injection into the cylinder. For the quantitative analysis, the tumble ratio, TKE, tumble-center travel path, and flow rotation intensity were compared with the results of in-cylinder flow obtained without injection.

In the case of injecting fuel, the mean and maximum velocities were found to be higher than those observed without fuel injection. This could be attributed to the additional momentum that was supplied by injecting fuel, as shown in Fig. 22. The mean velocity increased until bTDC 210°, although the mean velocity decreased faster than that without fuel

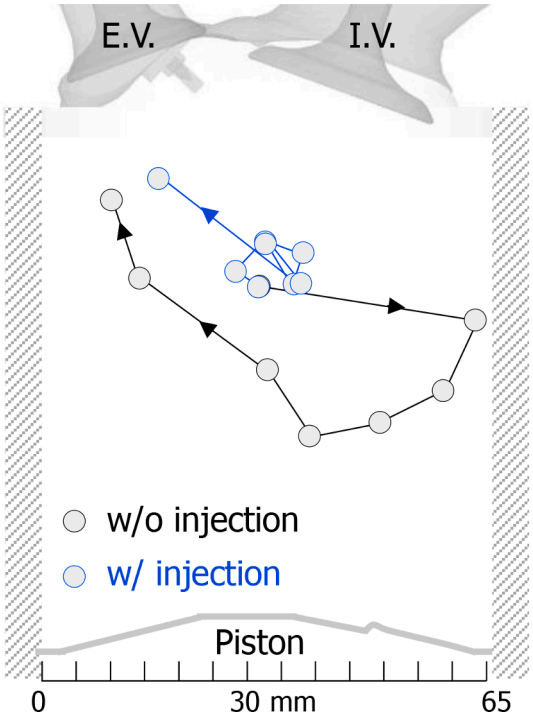

Fig. 24. Comparison of tumble-center travel path from bTDC 270° to bTDC 60° depending on fuel injection.

injection, which could be attributed to the fuel injected under a high injection pressure consisting of small droplets. The dissipation of momentum was fast in the case of small droplets with high momentum. Moreover, as the compression stroke progressed, the mean and maximum velocities under conditions with fuel injection were found to be similar to those obtained without fuel injection. This is because the in-cylinder flow loses its momentum owing to the continuous friction force.

The intensified in-cylinder flow was confirmed by the tumble ratio and TKE results, as depicted in Fig. 23. In Fig. 23(a), the tumble ratio obtained without injection exhibited a minimum at bTDC 150°. However, the tumble ratio with injection had a minimum at bTDC 120°. This could be attributed to the fact that the intensified tumble flow was maintained for a relatively longer time. In addition, the TKE increased when fuel was injected, as shown in Fig. 23(b). However, it significantly decreased with an increase in the crank angle. The reason for this is the same as that for the steeply decreasing in-cylinder flow velocity. Furthermore, in the compression stroke, the turbulent components were similar to those obtained without injection.

Fig. 24 shows the tumble-center travel path depending on the fuel injection. Without fuel injection, the tumble center began at the middle of the cylinder at bTDC 270°. Subsequently, it moved from the right to the left side in a semicircle. This implies that the dominant flow is at the left side in the intake stroke, while it is at the right side in the compression stroke. In contrast, tumble centers were concentrated in the middle of the cylinder after fuel injection. In these results, the in-cylinder flow was intensified by the injected fuel, and consequently, exhibited strong rotation based on the center of the cylinder.

The dependence of the flow rotation intensity on the fuel injection is shown in Fig. 25. The co-flow at the left side and the counter-flow on the right side intensified following fuel injection. Therefore, the in-cylinder flow exhibited strong rotation from the intake stroke to the early stage of the compression stroke. However, after bTDC 150°, the in-cylinder flow continued to rotate, but the counter-flow at the right side was stronger than the co-flow at the left side. Therefore, when multiple injections (double or triple injections) are applied, the effects of the first injection on the in-cylinder flow should be considered for the mixing performances of the second and third injections.

We varied the injection timing to confirm the effects of injection timing on in-cylinder flow. Fig. 26 shows the mean in-cylinder flow field at bTDC 90° depending on the injection timing. The injection timing was varied from bTDC 300° to bTDC 120° for both the intake and compression strokes. The in-cylinder flow at bTDC 90° was observed to be relatively less affected by fuel injection for an earlier injection timing. However, for injection timings of bTDC 150° and bTDC 120°, the in-cylinder flow at bTDC 90° exhibited a strong upward flow. Thus, the more delayed the injection timing, the stronger the flow moving toward the upper side of the cylinder. These results differ from those obtained for the side-mount injection, wherein the spray develops in only one direction. In the case of the side-mount type injector, owing to the high momentum being supplied in one direction, the in-cylinder flow rotates strongly in one direction [44].

The mean and maximum velocities are depicted in Fig. 27. The mean velocity at bTDC 90° with fuel injection was slightly higher than that without fuel injection, as shown in Fig. 27(a). However, the mean velocity was still lower than the piston speed until the injection timing of

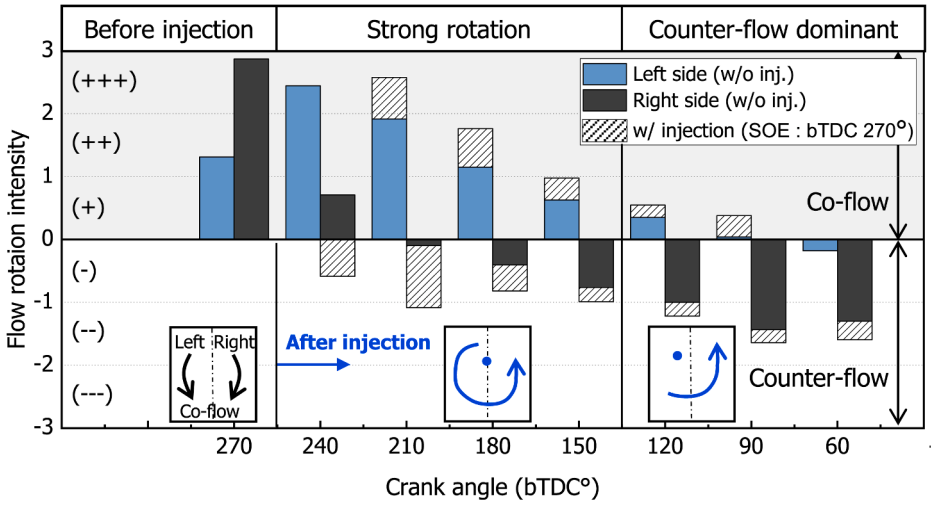

Fig. 25. Flow rotation intensity depending on fuel injection.

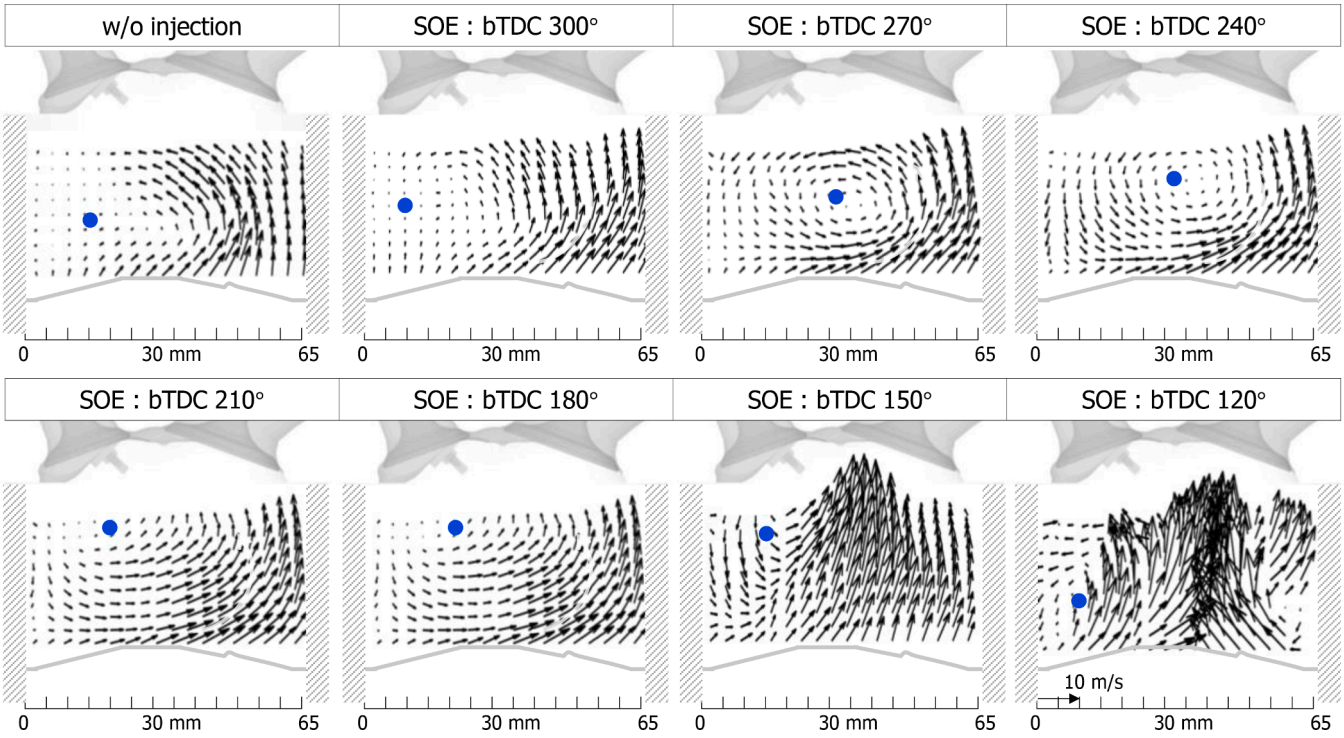

Fig. 26. Mean in-cylinder flow field at bTDC 90° depending on injection timing (@ 1,500 rpm, NA, P_{inj}:700 bar).

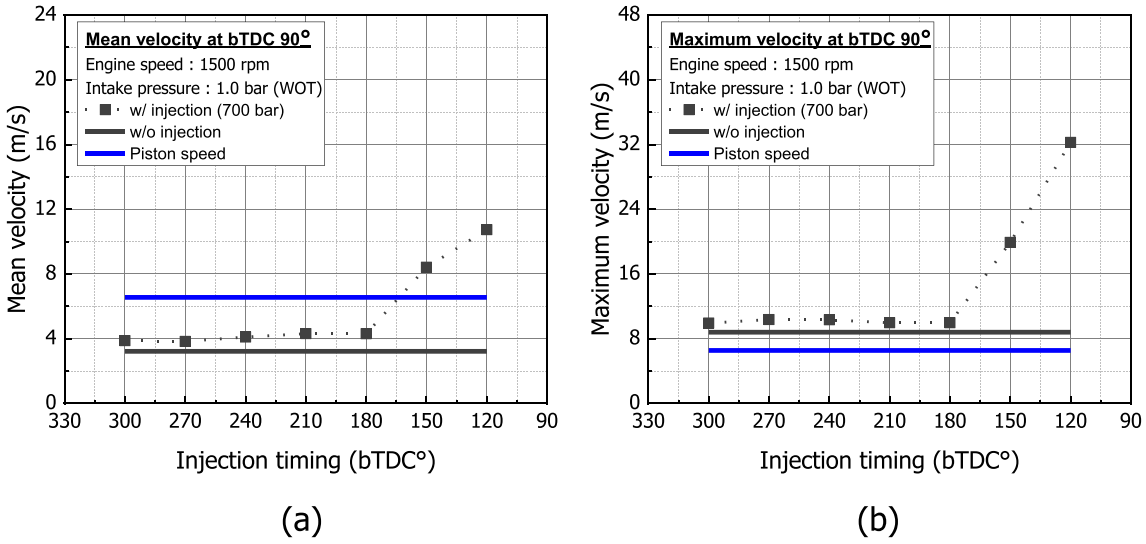

Fig. 27. Mean in-cylinder flow velocity at bTDC 90° depending on injection timing: (a) mean velocity and (b) maximum velocity.

bTDC 180°. This is because there is a relatively long time available following the end of injection in which the momentum of the in-cylinder flow decreases. The maximum velocity demonstrated the same tendency as that of the mean velocity; it increased significantly after the injection timing of bTDC 180°, as shown in Fig. 27(b). In this region, the dominant flow was the flow that occurred during spray development.

As depicted in Fig. 28(a), the tumble ratio increased after injecting fuel. In the case of the injection at bTDC 300°, there is a relatively long time available for the dissipation of the momentum; thus, the tumble ratio obtained with injection is similar to that obtained without it. In the cases of injection timings of bTDC 270° and bTDC 240°, a relatively strong co-flow existed, such that the in-cylinder flow was intensified by the interaction between the air and spray. In contrast, at injection timings of bTDC 210° and bTDC 180°, the co-flow was weak compared to the co-flow observed in the early stage of the intake stroke. Therefore, the in-cylinder flow was less intensified. Furthermore, after the injection timing of bTDC 180°, the in-cylinder flow was more affected by the fuel injection because the time available until bTDC 90° was less. Therefore, the tumble ratio rapidly increased after the injection timing of bTDC 180°. The TKE also significantly increased after bTDC 180°, as depicted in Fig. 28(b).

The results of the in-cylinder flow of the pent-roof region and tumble ratio are depicted in Figs. 29 and 30, respectively. The in-cylinder flow velocity near the TDC increased with the injection in all cases. This could

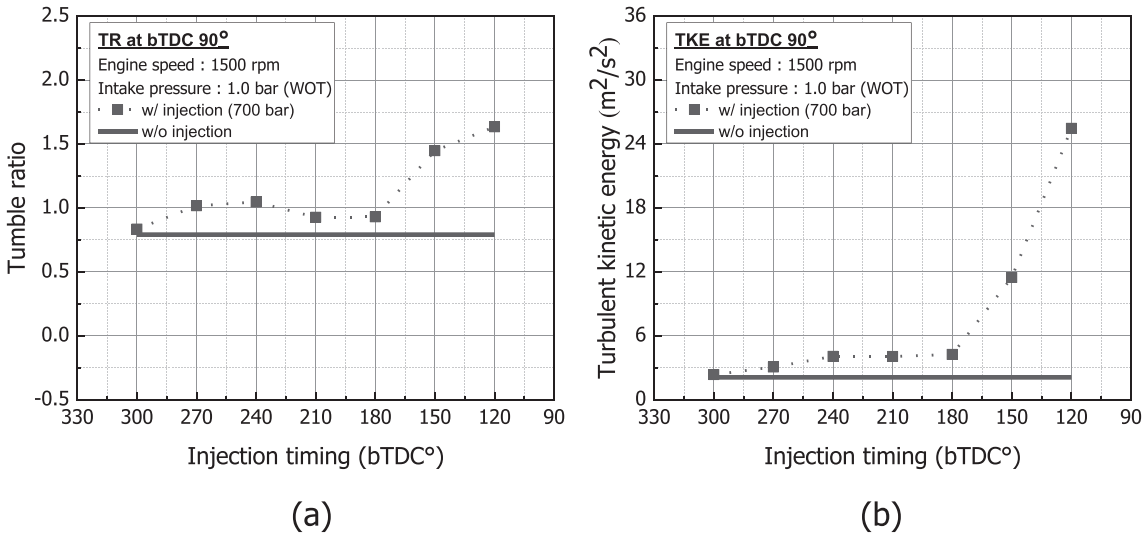

Fig. 28. Tumble ratio and TKE at bTDC 90° depending on injection timing: (a) tumble ratio and (b) TKE.

be attributed to the additional momentum supplied by the injected fuel. In particular, in the case where fuel was injected in region 3, the most intensified in-cylinder flow results were observed for the in-cylinder flow because it had lesser time available to dissipate the energy from injection until TDC.

The tumble variation with injection timing can be explained by considering the flow rotation intensity, which reveals the co-flow and counter-flow effects. In the case of the injection at bTDC 300°, the effects of the counter-flow on the left side, which rises upward by influencing the piston, and the co-flow on the right side due to the intake flow are offset. Thus, in this case, the tumble ratio after the end of injection was approximately the same as that without injection. However, in the case of the injection at bTDC 270°, a strong co-flow was generated in the cylinder and consequently, the tumble flow was enhanced by injection. In region 2, the co-flow effect weakened as the injection timing was retarded. However, the co-flow effect was still more dominant than the counter-flow effect. Thus, the tumble ratio decreased with retarded injection timing, but was higher than that obtained without injection. Moreover, in the case of injection in region 3, the counter-flow was dominant and the in-cylinder flow was disturbed by the spray. Therefore, after injection, the tumble ratio decreased more than without injection near the TDC.

In the case of injecting fuel, the TKE increased near the TDC, as depicted in Figs. 31 and 32. This is attributed to the turbulence supplied to the cylinder owing to the injection. The TKE at bTDC 20° continuously increased, as shown in Fig. 32, except for the injection timing of bTDC 90°, resulting from the spray targeting. In the case of injection in region 3, the injection timing was close to the TDC, such that the in-cylinder flow around the spark timing was affected by spray targeting.

For fuel injected in region 3, the spray targeting obtained was different, as depicted in Figs. 33 and 34. In the case of targeting the liner (e.g., SOE = bTDC 120°), the fuel collided with the surface of the liner, and consequently rotated toward the inner side of the cylinder causing the fuel flow to combine with the upward flow by the piston. Thus, the flow after injection was enhanced in the upward direction. In the case of targeting the liner and piston (e.g., SOE = bTDC 90°), the fuel was directly influenced by the upward movement of the piston, which was in the direction opposite to that of the spray during injection. Consequently, the momentum of the spray and in-cylinder flows was dissipated. Therefore, the injected fuel stagnated around the edge of the piston head. In the third case, where the spray targeted the piston bowl (e.g., SOE = bTDC 60°), the left side of the plume rotated toward the outside of the cylinder while the right side rotated toward the inside of the cylinder owing to the piston bowl shape. Subsequently, an upward flow was generated. Moreover, as a result of spray targeting, at SOE = bTDC 90°, the TKE at bTDC 20° was lower than that when fuel was injected at bTDC 120°, despite the retarded injection timing (Fig. 32).

4.3. Characteristics of the mixture formation process

The mixture characteristics for different injection timings can be determined by the in-cylinder flow following the end of injection because, during injection, the fuel momentum is strong such that the in-cylinder flow has little effect on the spray development. However, after the end of injection, the fuel evaporates, and the momentum supplied by the injection pressure is stopped. Therefore, the evaporated fuel travels with the in-cylinder flow, and consequently, this process determines the mixture characteristics.

Fig. 35 depicts the mixture formation process based on the end of injection timing. In the case of the EOI in region 1, the injected fuel was rotated by a strong tumble flow after the end of injection. Moreover, the fuel was over-mixed and eventually formed a homogeneous mixture at bTDC 20°, which was close to the spark timing. In contrast, in the case of the EOI in region 2, the injected fuel moved from the piston to the intake valve in the vicinity of the spark plug along the tumble flow. Thus, the fuel was located around the spark plug at bTDC 20° and consequently, a stratified mixture formation was generated at bTDC 20°. In region 3, the in-cylinder flow was weak owing to momentum dissipation during the compression stroke. Thus, in the case of the EOI in region 3, there was little time or insufficient in-cylinder flow to form a homogeneous or stratified mixture. Therefore, a mixture with a partially rich area, for example, a mal-distribution mixture, was formed. Thus, as depicted in Fig. 36, the mixture characteristics could be classified into homogeneous, stratified, and partially rich based on the in-cylinder flow characteristics at the end of the injection.

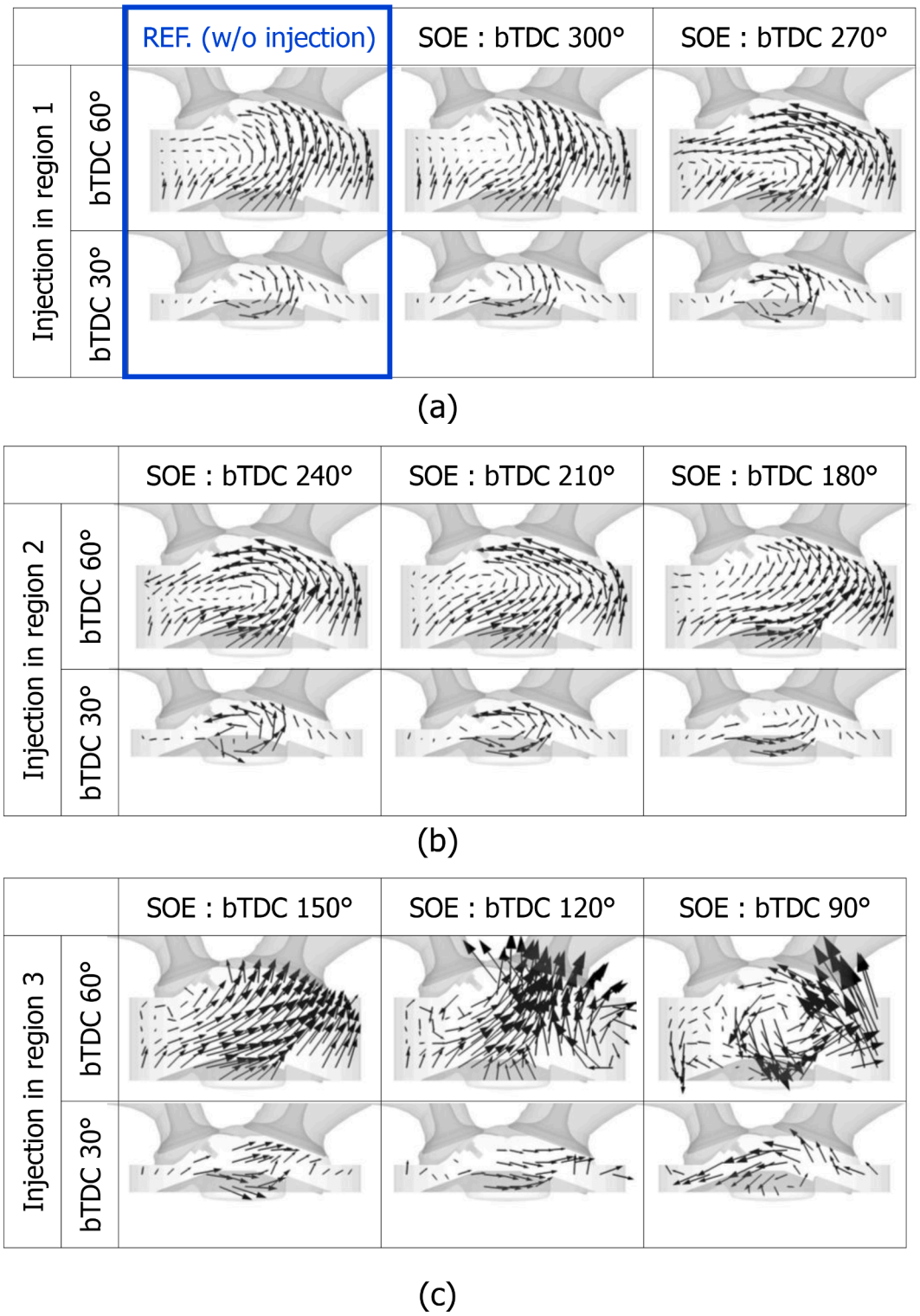

Fig. 29. CFD results of in-cylinder flow at bTDC 60° and bTDC 30° depending on injection timing: (a) injection in region 1, (b) region 2, and (c) region 3.

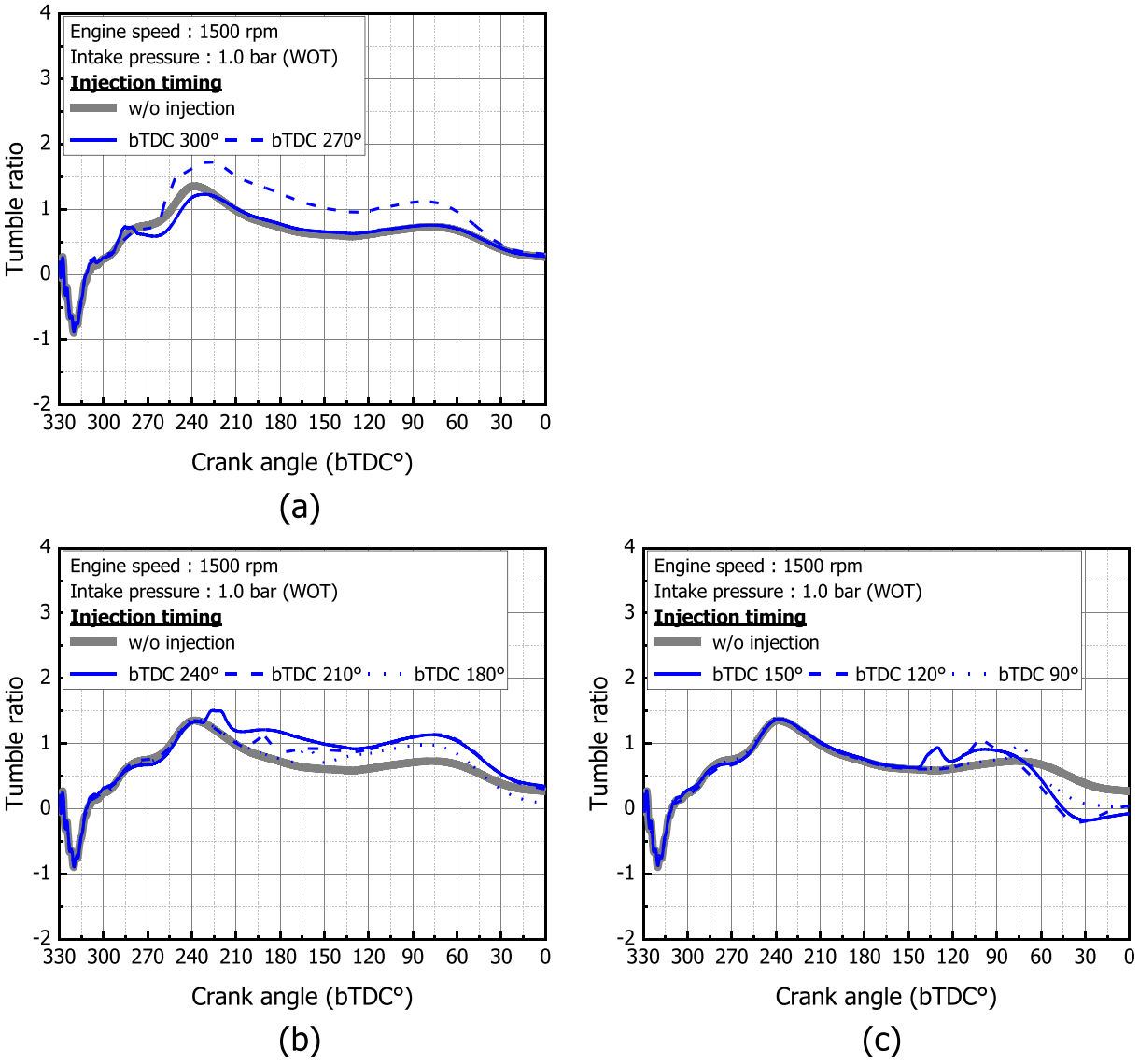

Fig. 30. CFD results of tumble ratio depending on injection timing: (a) injection in region 1, (b) region 2, and (c) region 3.

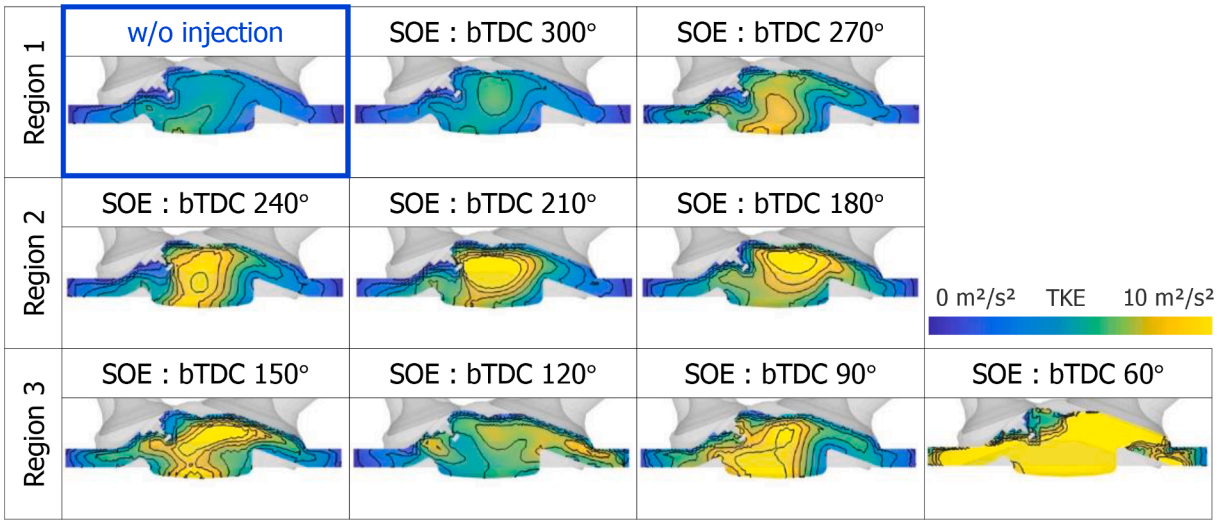

Fig. 31. CFD results showing the TKE distribution at bTDC 20° depending on injection timing (@ 1,500 rpm, N.A., P_{inj}:700 bar, lambda:1).

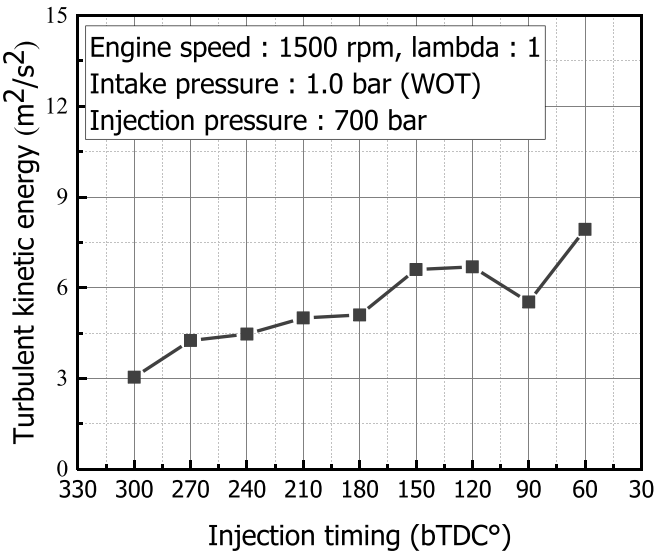

Fig. 32. CFD results of TKE at bTDC 20° depending on injection timing.

5. Conclusions

In this study, the characteristics of in-cylinder flow and mixture formation were investigated using PIV measurements and CFD in an optically accessible 2-cylinder GDI engine that applied center-mounted-type high-pressure injectors. Furthermore, the interactions between the spray and in-cylinder flows were studied. Consequently, the following conclusions were drawn:

1. We defined the flow that had the same direction as that of the spray development as co-flow and the flow that had the opposite direction to that of the spray development as counter-flow. Furthermore, the flow characteristics depending on the crank angle were divided into regions 1, 2, and 3. Region 1 was before bTDC 270°, wherein strong co-flow occurred on the right side of the cylinder. Region 2 was from bTDC 240° to bTDC 180°, wherein tumble flow occurred, resulting in co-flow on the left side of the cylinder and counter-flow on the right side of the cylinder. Region 3 was after bTDC 150°, wherein counter-flow was dominant on the right side of the cylinder. During the intake compression stroke, the momentum supplied at the early stage of the intake stroke was constantly lost, resulting in a continuous decrease in the in-cylinder flow velocity and TKE.
2. The spray structure was influenced by the in-cylinder flow. In region 1, wherein a strong in-cylinder flow was formed, the interaction between the spray and air increased, causing the spray to scatter. However, no clear spray collapse was observed. Moreover, the spray scattering decreased as the in-cylinder flow weakened.
3. The in-cylinder flow was intensified with the injection of the fuel because of the additional momentum supplied by the injection. Therefore, the in-cylinder flow velocity, tumble ratio, and turbulent kinetic energy increased compared to the results obtained without fuel injection.
4. The mixture formation was significantly influenced by the injection timing, particularly at the end of the injection timing. A homogeneous mixture was formed as the injection was stopped in region 1 because the in-cylinder flow had strong momentum, and there was a relatively long time available for the air and fuel to mix. The stratified mixture was obtained when the end of the injection timing was in region 2. Finally, at the end of the injection timing in region 3, a mal-distribution was generated owing to the high in-cylinder pressure and weak in-cylinder flow.

CRediT authorship contribution statement

Donghwan Kim: Writing – original draft, Investigation. **Jisoo Shin:** Investigation. **Yousang Son:** Investigation. **Sungwook Park:** Writing - review & editing, Supervision.

Declaration of Competing Interest

The authors declare that they have no known competing financial interests or personal relationships that could have appeared to influence the work reported in this paper.

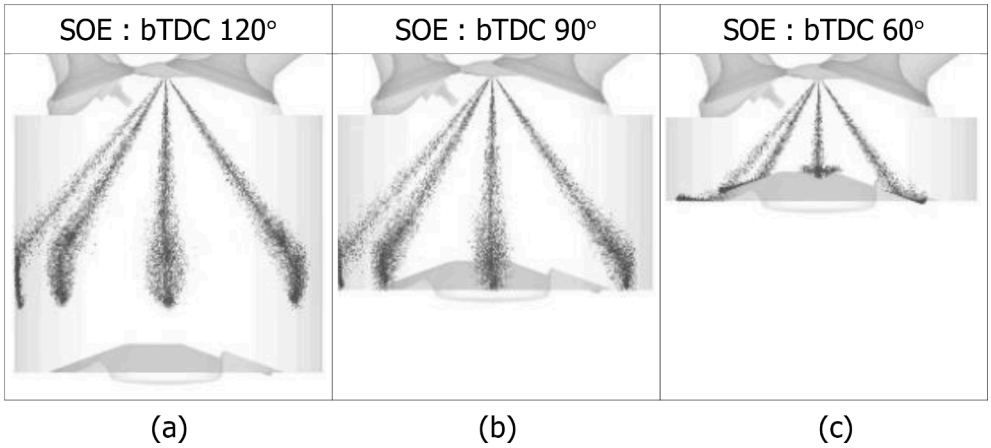

Fig. 33. Spray targeting depending on injection timing in region 3: (a) targeting the liner, (b) targeting the liner and piston, and (c) targeting the piston head.

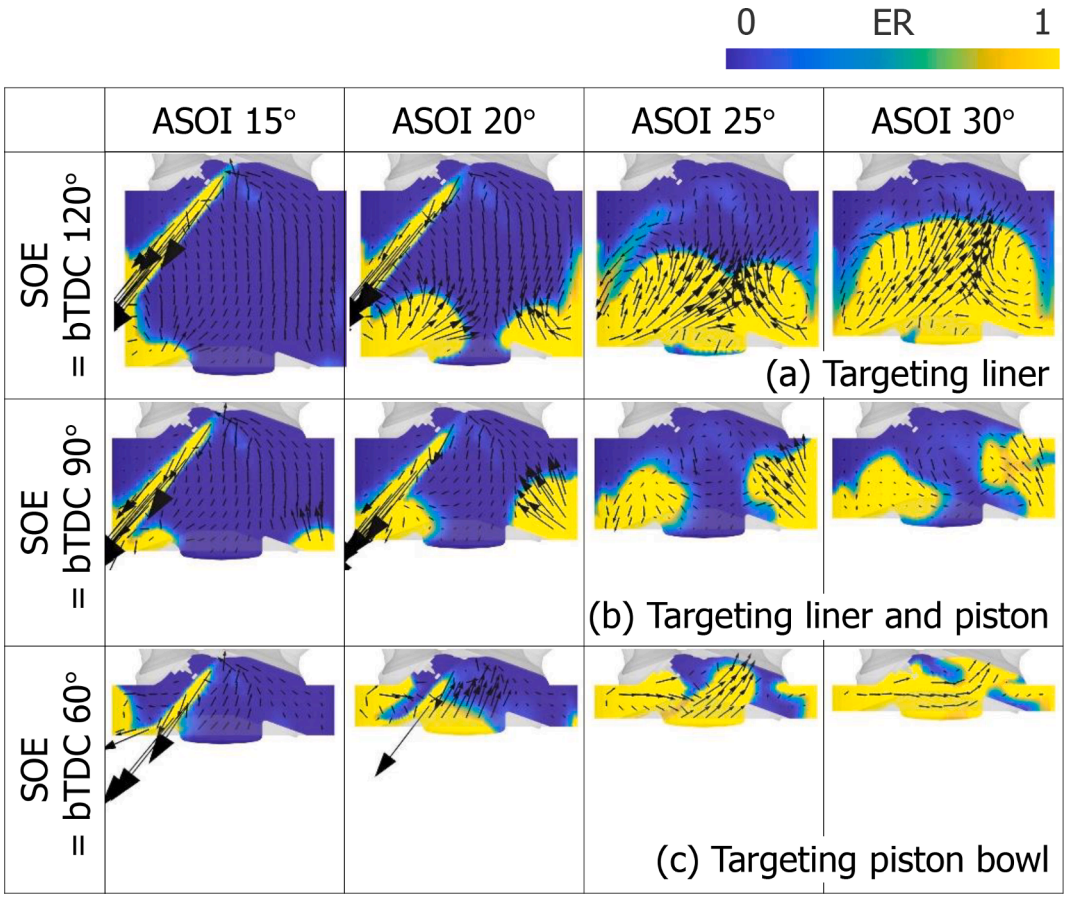

Fig. 34. Mixture formation process depending on spray targeting location (@ 1,500 rpm, NA, P_{inj}:700 bar, lambda:1).

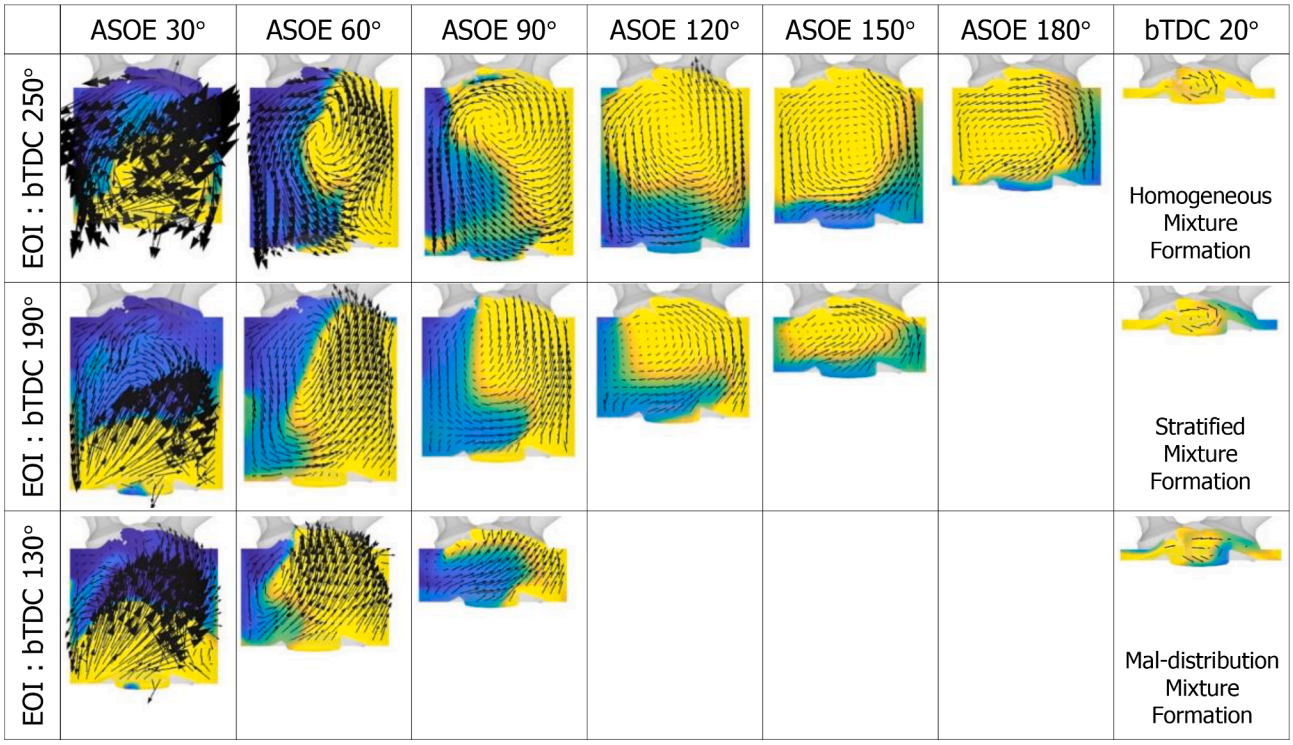

Fig. 35. Mixture formation process depending on end of injection timing (@ 1,500 rpm, NA, P_{inj}:700 bar, lambda:1).

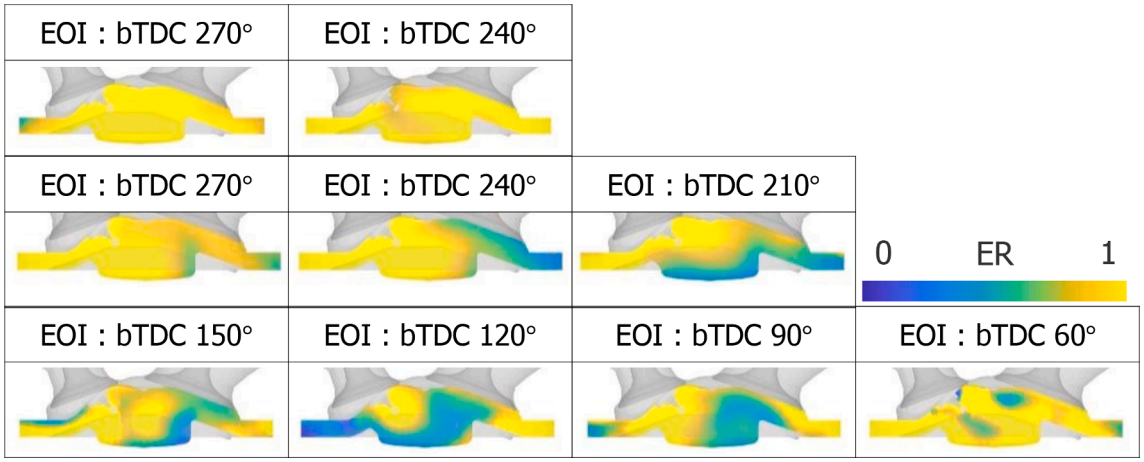

Fig. 36. Equivalence ratio distribution depending on EOI (@ 1,500 rpm, NA, P_{inj}:700 bar, lambda:1).

Acknowledgement

This work was supported by the Engine Advanced Development Team of Hyundai Motor Group and by the National Research Foundation of Korea (NRF) grant funded by the Korean government (MSIT). (2021R1A2C2011425)

References

[1] Hannan MA, Azidin FA, Mohamed A. Hybrid electric vehicles and their challenges: A review. Renew Sustain Energy Rev 2014;29:135–50. https://doi.org/10.1016/j.rser.2013.08.097.
[2] Sabri MFM, Danapalasingam KA, Rahmat MF. A review on hybrid electric vehicles architecture and energy management strategies. Renew Sustain Energy Rev 2016;53:1433–42. https://doi.org/10.1016/j.rser.2015.09.036.
[3] Kester J, Noel L, Zarazua de Rubens G, Sovacool BK. Policy mechanisms to accelerate electric vehicle adoption: A qualitative review from the Nordic region. Renew Sustain Energy Rev 2018;94:719–31. https://doi.org/10.1016/j.rser.2018.05.067.
[4] Hwang J-J. Sustainability study of hydrogen pathways for fuel cell vehicle applications. Renew Sustain Energy Rev 2013;19:220–9. https://doi.org/10.1016/j.rser.2012.11.033.
[5] Hao X, Wang H, Lin Z, Ouyang M. Seasonal effects on electric vehicle energy consumption and driving range: A case study on personal, taxi, and ridesharing vehicles. J Cleaner Prod 2020;249:119403. https://doi.org/10.1016/j.jclepro.2019.119403.
[6] Dudley, B., BP statistical review of world energy. BP Statistical Review, London, UK, accessed Aug, 2018. 6(2018): p. 00116.
[7] Heywood JB. Internal combustion engine fundamentals. McGraw-Hill Education; 2018.
[8] Fansler TD, Reuss DL, Sick V, Dahms RN. Invited review: Combustion instability in spray-guided stratified-charge engines: A review. Int J Engine Res 2015;16(3):260–305. https://doi.org/10.1177/1468087414565675.
[9] Li X, Sjöberg M, Vuilleumier D, Ding C-P, Liu F, et al. Impact of coolant temperature on piston wall-wetting and smoke generation in a stratified-charge DISI engine operated on E30 fuel. Proc Combust Inst 2019;37(4):4955–63. https://doi.org/10.1016/j.proci.2018.07.073.
[10] Duan X, Lai M-C, Jansons M, Guo G, Liu J. A review of controlling strategies of the ignition timing and combustion phase in homogeneous charge compression ignition (HCCI) engine. Fuel 2021;285:119142. https://doi.org/10.1016/j.fuel.2020.119142.
[11] Hasan MM, Rahman MM. Homogeneous charge compression ignition combustion: Advantages over compression ignition combustion, challenges and solutions. Renew Sustain Energy Rev 2016;57:282–91. https://doi.org/10.1016/j.rser.2015.12.157.
[12] Liu H, Zhang P, Li Z, Luo J, Zheng Z, Yao M. Effects of temperature inhomogeneities on the HCCI combustion in an optical engine. Appl Therm Eng 2011;31(14-15):2549–55. https://doi.org/10.1016/j.applthermaleng.2011.04.020.
[13] Jamsran N, Putrasari Y, Lim O. A computational study on the autoignition characteristics of an HCCI engine fueled with natural gas. J Nat Gas Sci Eng 2016;29:469–78. https://doi.org/10.1016/j.jngse.2016.01.008.
[14] Panão MRO, Moreira ALN. Interpreting the influence of fuel spray impact on mixture preparation for HCCI combustion with port-fuel injection. Proc Combust Inst 2007;31(2):2205–13. https://doi.org/10.1016/j.proci.2006.07.050.
[15] Li G, Zhang C, Zhou J. Study on the knock tendency and cyclical variations of a HCCI engine fueled with n-butanol/n-heptane blends. Energy Convers Manage 2017;133:548–57. https://doi.org/10.1016/j.enconman.2016.10.074.
[16] Wang T, Zhang X, Zhang J, Hou X. Numerical analysis of the influence of the fuel injection timing and ignition position in a direct-injection natural gas engine. Energy Convers Manage 2017;149:748–59. https://doi.org/10.1016/j.enconman.2017.03.004.
[17] Baratta M, Misul D, Xu J. Development and application of a method for characterizing mixture formation in a port-injection natural gas engine. Energy Convers Manage 2021;227:113595. https://doi.org/10.1016/j.enconman.2020.113595.
[18] Costa M, Sorge U, Allocca L. Increasing energy efficiency of a gasoline direct injection engine through optimal synchronization of single or double injection strategies. Energy Convers Manage 2012;60:77–86. https://doi.org/10.1016/j.enconman.2011.12.025.
[19] Das P, Subbarao P, Subrahmanyam J. Effect of main injection timing for controlling the combustion phasing of a homogeneous charge compression ignition engine using a new dual injection strategy. Energy Convers Manage 2015;95:248–58. https://doi.org/10.1016/j.enconman.2015.02.018.
[20] Lee Z, Kim D, Park S. Effects of spray behavior and wall impingement on particulate matter emissions in a direct injection spark ignition engine equipped with a high pressure injection system. Energy Convers Manage 2020;213:112865. https://doi.org/10.1016/j.enconman.2020.112865.
[21] Heywood, J.B., Fluid motion within the cylinder of internal combustion engines—the 1986 Freeman scholar lecture. 1987.
[22] Zeng W, Sjöberg M, Reuss DL. PIV examination of spray-enhanced swirl flow for combustion stabilization in a spray-guided stratified-charge direct-injection spark-ignition engine. Int J Engine Res 2014;16(3):306–22. https://doi.org/10.1177/1468087414564605.
[23] Geschwindner C, Kranz P, Welch C, Schmidt M, Böhm B, Kaiser SA, et al. Analysis of the interaction of Spray G and in-cylinder flow in two optical engines for late gasoline direct injection. Int J Engine Res 2020;21(1):169–84. https://doi.org/10.1177/1468087419881535.
[24] Hill H, Ding C-P, Baum E, Böhm B, Dreizler A, Peterson B. An application of tomographic PIV to investigate the spray-induced turbulence in a direct-injection engine. Int J Multiph Flow 2019;121:103116. https://doi.org/10.1016/j.ijmultiphaseflow.2019.103116.
[25] da Costa RBR, Braga RM, Gomes Júnior CA, Valle RM, Huebner R. PIV measurements and numerical analysis of in-cylinder tumble flow in a motored engine. J Braz Soc Mech Sci Eng 2017;39(10):3931–45.
[26] Thielicke W, Stamhuis EJ, PIVlab – Towards user-friendly, affordable and accurate digital particle image velocimetry in MATLAB. J Open Res Softw, 2014. 2., Doi: 10.5334/jors.bl.
[27] Nogueira J, Lecuona A, Rodríguez PA. Data validation, false vectors correction and derived magnitudes calculation on PIV data. Meas Sci Technol 1997;8(12):1493–501. https://doi.org/10.1088/0957-0233/8/12/012.
[28] Raffel M, et al. Particle image velocimetry: A practical guide. Springer; 2018.
[29] Stansfield P, Wigley G, Justham T, Catto J, Pitcher G. PIV analysis of in-cylinder flow structures over a range of realistic engine speeds. Exp Fluids 2007;43(1):135–46. https://doi.org/10.1007/s00348-007-0335-x.
[30] Salazar V, Kaiser S. Interaction of intake-induced flow and injection jet in a direct-injection hydrogen-fueled engine measured by PIV. SAE Technical Paper Series 2011. https://doi.org/10.4271/2011-01-0673.
[31] Reitz RD, Beale JC. Modeling spray atomization with the Kelvin-Helmholtz/Rayleigh-Taylor hybrid model. Atom Sprays 1999;9(6):623–50. https://doi.org/10.1615/AtomizSpr.v9.i6.40.
[32] Kumar Agarwal A, Gadekar S, Pratap Singh A. In-cylinder flow evolution using tomographic particle imaging velocimetry in an internal combustion engine. J Energy Res Technol 2018;140(1). https://doi.org/10.1115/1.4037686.
[33] Dannemann J, Klaas M, Schröder W. Three dimensional flow field within a four valve combustion engine measured by particle-image velocimetry. ISFV 2010.
[34] Liu Y, et al. Numerical simulation on spray atomization and fuel-air mixing process in a gasoline direct injection engine. SAE Technical Paper Series 2012. https://doi.org/10.4271/2012-01-0395.

[35] Ghasemi A, Li X, Hong Z, Yun S. Breakup mechanisms in air-assisted atomization of highly viscous pyrolysis oils. Energy Convers Manage 2020;220:113122. https://doi.org/10.1016/j.enconman.2020.113122.
[36] Kim T, Song J, Park J, Park S. Numerical and experimental study on effects of fuel injection timings on combustion and emission characteristics of a direct-injection spark-ignition gasoline engine with a 50 MPa fuel injection system. Appl Therm Eng 2018;144:890–900. https://doi.org/10.1016/j.applthermaleng.2018.09.007.
[37] Chen Z, Chen H, Wang L, Geng L, Zeng K. Parametric study on effects of excess air/fuel ratio, spark timing, and methanol injection timing on combustion characteristics and performance of natural gas/methanol dual-fuel engine at low loads. Energy Convers Manage 2020;210:112742. https://doi.org/10.1016/j.enconman.2020.112742.
[38] Iwamoto Y, et al., Development of gasoline direct injection engine. 1997, SAE Technical Paper. doi: 10.4271/1999-01-2938.
[39] Alkidas AC. Combustion advancements in gasoline engines. Energy Convers Manage 2007;48(11):2751–61. https://doi.org/10.1016/j.enconman.2007.07.027.
[40] Guo M, Shimasaki N, Nishida K, Ogata Y, Wada Y. Experimental study on fuel spray characteristics under atmospheric and pressurized cross-flow conditions. Fuel 2016;184:846–55. https://doi.org/10.1016/j.fuel.2016.07.083.
[41] Roisman IV, Araneo L, Tropea C. Effect of ambient pressure on penetration of a diesel spray. Int J Multiph Flow 2007;33(8):904–20. https://doi.org/10.1016/j.ijmultiphaseflow.2007.01.004.
[42] Zama Y, Ochiai W, Furuhata T, Arai M. Experimental study on spray angle and velocity distribution of diesel spray under high ambient pressure conditions. Atom Sprays 2011;21(12). https://doi.org/10.1615/AtomizSpr.2012004722.
[43] Leong MY, McDonell VG, Samuelsen GS. Effect of ambient pressure on an airblast spray injected into a crossflow. J Propul Power 2001;17(5):1076–84. https://doi.org/10.2514/2.5846.
[44] Sevik J, Pamminger M, Wallner T, Scarcelli R, Boyer B, Wooldridge S, et al. Influence of injector location on part-load performance characteristics of natural gas direct-injection in a spark ignition engine. SAE Int J Engines 2016;9(4):2262–71. https://doi.org/10.4271/2016-01-2364.